https://doi.org/10.5194/egusphere-2026-5387
Preprint. Discussion started: 24 November 2026
© Author(s) 2026. CC BY 4.0 License.

Evolution of black carbon heterogeneity and optical absorption during atmospheric aging

Qiqi Mo[1], Jie Sun[1], Tong Liu[1], Gang Zhao[1*], Fengjun Shen[1], Xinlei Lv[1], Ziye Zhang[1], Yunxiao Li[1], Batu Alaxi[1], Weili Lin[1, 2]

1Key Laboratory of Ecology and Environment in Minority Areas, Minzu University of China, National Ethnic Affairs Commission, Beijing 100081, China
2Institute of National Security, Minzu University of China, Beijing, 100081, China

Correspondence to: Gang Zhao (gangz@muc.edu.cn)

Abstract

Black carbon (BC) mixing state evolves through emissions, chemical ageing, boundary-layer variation, and coagulation, but their distinct effects on BC heterogeneity and optical properties remain poorly quantified. We combined size-resolved BC core and coating measurements in suburban Taizhou (Yangtze River Delta, China) with observation-constrained simulations using the coupled Particle Monte Carlo model and Model for Simulating Aerosol Interactions and Chemistry (PartMC–MOSAIC) and core–shell Mie calculations. Campaign-mean coating-to-BC mass ratio (MR), mixing-state index (χ), average particle diversity (D_α), and population diversity (D_γ) were 2.63 ± 0.62, 0.73 ± 0.03, 1.54 ± 0.06, and 1.74 ± 0.06, respectively. D_α, D_γ, and χ increased after 16:00 without a comparable MR increase, indicating redistribution of non-BC material rather than greater bulk coating mass. Relative to process-free χ (0.79), chemical ageing increased mean χ by 11.9 %, whereas fresh emissions decreased it by 32.6 %; boundary-layer variation and coagulation changed mean χ little but followed distinct D_α-D_γ trajectories. Fresh emissions increased the mean absorption coefficient (σ_{abs}) by 48.4 % but reduced absorption enhancement (E_{abs}) by 12.2 %, whereas chemical ageing increased them by 28.3 % and 27.1 %, respectively; coagulation increased Eabs by 4.4 %. Under the simulated conditions, BC loading primarily influenced σabs, whereas coating amount and its particle-to-particle distribution more strongly affected Eabs. Distinct D_α-D_γ trajectories and contrasting optical responses highlight the value of combining mixing-state diversity and optical metrics to identify process-specific BC evolution.

1 Introduction

Black carbon (BC) is one of the strongest light-absorbing components of atmospheric aerosol. It heats the atmosphere by absorbing solar radiation, perturbs the surface-atmosphere energy balance, and can subsequently affect boundary-layer development, photochemistry, and cloud processes. After deposition on snow and ice, BC can produce additional warming by reducing surface albedo (Fierce et al., 2020; Wang et al., 2017). These environmental and

https://doi.org/10.5194/egusphere-2026-5387
Preprint. Discussion started: 24 November 2026
© Author(s) 2026. CC BY 4.0 License.

climatic effects depend not only on BC mass concentration but also on its mass-specific absorption efficiency. Following emission, BC undergoes atmospheric aging through condensation, coagulation, and heterogeneous reactions, during which organic and inorganic materials accumulate on the BC surface. The resulting lensing effect can enhance BC absorption. However, absorption enhancement (E_{abs}) factors derived from laboratory experiments, field observations, and model calculations differ considerably (Cappa et al., 2019; Liu et al., 2017; Cappa et al., 2012). This discrepancy limits accurate estimates of BC absorption and radiative effects. Understanding the coupled evolution of BC microphysical and optical properties during atmospheric aging is therefore important.

The optical response of BC is influenced by the morphology and size of the BC core, the amount and composition of its coating, and the mixing state of the particle population (Wu et al., 2018; Wang et al., 2021). Ambient BC populations contain particles originating from different sources and experiencing different degrees of atmospheric aging. Individual particles can therefore differ substantially in coating thickness and BC mass fraction, even when the population has a well-defined mean coating amount. Representing all BC-containing particles using an identical mean composition cannot capture this particle-to-particle heterogeneity and may bias estimates of absorption and radiative effects (Fierce et al., 2016; Fierce et al., 2020; Huang et al., 2024). Indeed, BC populations with similar bulk coating amounts can exhibit different absorption enhancements when the coating material is distributed differently among particles (Zeng et al., 2024; Zhao et al., 2021). Quantifying the distribution of coating material among individual BC-containing particles is therefore essential for linking population-level coating properties to BC absorption enhancement.

The entropy-based aerosol mixing-state framework proposed by Riemer and West (2013) provides a quantitative description of particle-to-particle compositional variability. Within this framework, D_α represents the average compositional diversity of individual particles, whereas D_γ represents the compositional diversity of the entire particle population. These two quantities are combined to obtain the mixing-state index (χ). A population approaches an externally mixed state and χ approaches 0 when chemical components are segregated among different particles, whereas χ approaches 1 when all particles have the same relative composition. This framework has been applied to single-particle measurements and particle-resolved simulations of ambient aerosols and BC-containing particles (Healy et al., 2014; Dickau et al., 2016; Yu et al., 2020). Observations have revealed substantial differences in BC mixing state among urban, suburban, rural, and background environments (Zhao et al., 2022). Even at the same bulk coating level, differences in particle-to-particle mixing-state heterogeneity can lead to uncertainties exceeding 20 % in E_{abs}, reaching approximately 24 % under highly coated conditions (Zhao et al., 2021; Zeng et al., 2024). However, these diversity metrics describe the distribution of chemical components within a particle population and do not directly encode BC loading, total coating amount, or particle size. Similar values of χ may therefore correspond to particle populations with different compositional structures and optical properties.

https://doi.org/10.5194/egusphere-2026-5387
Preprint. Discussion started: 24 November 2026
© Author(s) 2026. CC BY 4.0 License.

Different atmospheric processes can modify the BC mixing state through distinct and potentially competing pathways. Fresh emissions typically introduce thinly coated BC particles into an aged background population, thereby increasing particle-type diversity and particle-to-particle compositional differences (Liu et al., 2014). Secondary material formed through condensation and gas–particle reactions modifies the composition of BC-containing particles. When broadly distributed across the population, such material can make BC-containing particles more homogeneous, although the response depends on its partitioning among individual particles (Lee et al., 2019). Coagulation produces new mixing states by merging particles with different sizes and compositions and redistributes particle number and mass in size–composition space (Zaveri et al., 2010), whereas boundary-layer evolution and dilution further modulate the observed mixing state by altering background-particle entrainment, the dilution of near-surface emissions, and the relative contributions of particles with different source and aging histories (Riemer et al., 2009).

Despite the extensive work summarized above, our understanding of the atmospheric evolution of BC heterogeneity remains largely based on statistical relationships derived from field observations (Liu et al., 2014; Tan et al., 2021; Zhao et al., 2022) or on particle-resolved simulations in which multiple atmospheric processes operate simultaneously (Zhang et al., 2025; Fierce et al., 2016). The individual effects of fresh emissions, chemical aging, boundary-layer variation, and coagulation on BC diversity metrics have not yet been systematically compared within a consistent framework. It therefore remains unclear whether different processes can produce similar responses in D_α, D_γ, and χ, and whether the processes governing BC heterogeneity exert corresponding effects on the bulk absorption coefficient (σ_{abs}) and absorption enhancement (E_{abs}). This knowledge gap limits the process-based representation of BC mixing-state and optical evolution in atmospheric models and contributes to uncertainty in estimates of BC radiative effects.

To address this gap, we combined size-resolved BC core and coating measurements from Taizhou in the Yangtze River Delta with observation-constrained PartMC-MOSAIC simulations and core–shell Mie calculations. Accordingly, this study aims to (i) characterize the temporal evolution of average particle diversity (D_α), bulk population diversity (D_γ) and the BC mixing-state index (χ); (ii) isolate and quantify the effects of fresh emissions, chemical aging, boundary-layer variation, and coagulation on BC mixing-state evolution; (iii) assess how these process-specific changes influence the bulk absorption coefficient σ_{abs} and absorption enhancement (E_{abs}). By distinguishing changes in σ_{abs} associated mainly with BC loading from variations in E_{abs} associated with particle-scale coating and mixing structure, this study provides a process-level understanding of the link between BC mixing-state evolution and its optical response.

https://doi.org/10.5194/egusphere-2026-5387
Preprint. Discussion started: 24 November 2026
© Author(s) 2026. CC BY 4.0 License.

2 Methods

2.1 Sampling site

As shown in Fig. 1, the study site is located at the Taizhou Meteorological Radar Station (32°3′ N, 120° E) in suburban Taizhou, Jiangsu Province, at the southern edge of the Jianghuai Plain within the Yangtze River Delta (YRD), between the major cities of Nanjing and Shanghai. Field measurements were conducted from 26 May to 18 June 2018. The surrounding area is dominated by farmland, providing a suitable setting for investigating suburban aerosol characteristics in the YRD (Zhao et al., 2019). Although the site is relatively distant from major industrial facilities, the observations may still be influenced by anthropogenic emissions and regional transport within the YRD (Li et al., 2021). In addition, biomass-burning activities during the local crop-harvest season may intermittently affect aerosol properties (Liu et al., 2021). These environmental characteristics facilitate the investigation of the evolution of black carbon mixing state and optical properties under the combined influences of suburban background conditions, regional transport, and episodic emissions.

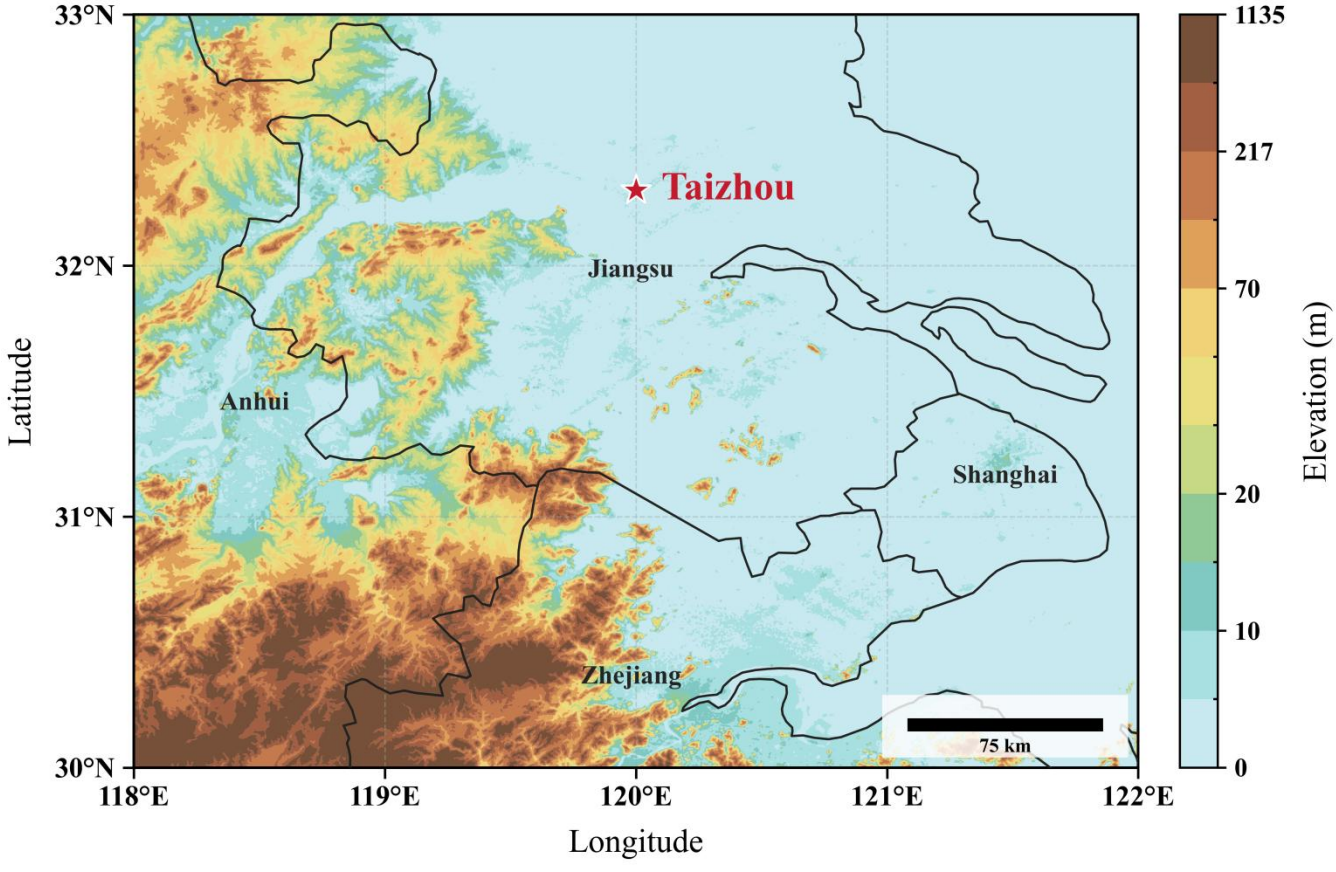

Figure 1: Location of the Taizhou observation site and surrounding topography. The red star denotes the observation site.

https://doi.org/10.5194/egusphere-2026-5387
Preprint. Discussion started: 24 November 2026
© Author(s) 2026. CC BY 4.0 License.

2.2 Instrumentation

In this study, all instruments were operated in a temperature-controlled container maintained at 22–26 °C. Ambient aerosol was sampled through a PM_{10} impactor mounted approximately 5 m above ground level and dried using a Nafion dryer. Size-resolved BC core diameter and non-BC coating thickness were measured using a differential mobility analyzer (DMA; model 3081, TSI Inc., USA) coupled with a single-particle soot photometer (SP2; Droplet Measurement Technologies, USA), which quantified refractory BC mass using laser-induced incandescence signals. The DMA – SP2 data were processed following the procedure described by Zhao et al. (2021). The aerosol scattering coefficient (σ_{sca}) was measured using an integrating nephelometer (Aurora 300, Ecotech, Australia). The aerosol absorption coefficient (σ_{abs}) was measured at a 1 min resolution using a seven-wavelength aethalometer (AE33, Magee Scientific, USA) at 370, 470, 520, 590, 660, 880, and 950 nm. Because the contribution of brown carbon absorption is relatively small at 880 nm, this channel was selected as the reference wavelength for characterizing BC absorption (Sun et al., 2026). Particle number size distributions over the diameter range of 20–800 nm were measured at a 5 min time resolution using a scanning mobility particle sizer (SMPS; model 3080, TSI Inc., USA). Ambient temperature (T), relative humidity (RH), wind speed (WS) and wind direction (WD) were continuously monitored using an automatic weather station (Met One Instruments Inc., USA).

2.3 Calculation of mixing state metrics

The mixing state of BC-containing particles was quantified using the information-theoretic framework introduced by Riemer and West (2013). This framework characterizes the distribution of chemical components among individual particles and has been used to investigate changes in the BC mixing state caused by emission, condensation, coagulation, dilution, and removal processes (Riemer et al., 2009; Zaveri et al., 2010; Zhang et al., 2025). Following Zhao et al. (2021) and Yao et al. (2022), particle composition was simplified into a binary system consisting of BC and non-BC coating material. The non-BC component represents the sum of all aerosol species other than BC. Only BC-containing computational particles were included; therefore, the resulting metric describes the distributional uniformity of non-BC coating material within the BC-containing particle population.

For each BC-containing computational particle i, the BC mass fraction was calculated as

$$p_{i,\mathrm{BC}} = \frac{m_{i,\mathrm{BC}}}{m_i} \tag{1}$$

where $m_{i,\mathrm{BC}}$ and m_i are the BC mass and total dry aerosol mass represented by particle i, respectively. The total BC mass and total aerosol mass of the BC-containing particle population were calculated as

$$m_{\mathrm{BC}} = \sum_{i=1}^{N} m_{i,\mathrm{BC}} \tag{2}$$

$$m_{\mathrm{tot}} = \sum_{i=1}^{N} m_i \tag{3}$$

https://doi.org/10.5194/egusphere-2026-5387
Preprint. Discussion started: 24 November 2026
© Author(s) 2026. CC BY 4.0 License.

where N is the number of BC-containing computational particles included in the calculation. The bulk BC mass fraction was then obtained from

$$p_{\mathrm{BC}} = \frac{m_{\mathrm{BC}}}{m_{\mathrm{tot}}} \tag{4}$$

The bulk mass ratio of non-BC coating material to BC was calculated as

$$MR = \frac{m_{\mathrm{tot}} - m_{\mathrm{BC}}}{m_{\mathrm{BC}}} = \frac{1 - p_{\mathrm{BC}}}{p_{\mathrm{BC}}} \tag{5}$$

The mass contribution of particle i to the total BC-containing particle population was defined as

$$p_i = \frac{m_i}{m_{\mathrm{tot}}} \tag{6}$$

The mixing entropy of particle i was calculated as

$$H_i = -\left[p_{i,\mathrm{BC}} \ln p_{i,\mathrm{BC}} + \left(1 - p_{i,\mathrm{BC}}\right) \ln \left(1 - p_{i,\mathrm{BC}}\right)\right] \tag{7}$$

The mass-weighted average particle mixing entropy, H_α, and the bulk population mixing entropy, H_γ, were calculated as

$$H_\alpha = \sum_{i=1}^{N} p_i H_i \tag{8}$$

$$H_\gamma = -\left[p_{\mathrm{BC}} \ln p_{\mathrm{BC}} + (1 - p_{\mathrm{BC}}) \ln (1 - p_{\mathrm{BC}})\right] \tag{9}$$

respectively. Here, ln denotes the natural logarithm, and $0 \ln 0$ is defined as zero.

The corresponding average particle species diversity and bulk population species diversity were obtained as

$$D_\alpha = e^{H_\alpha} \tag{10}$$

$$D_\gamma = e^{H_\gamma} \tag{11}$$

Finally, the BC mixing-state index was calculated as

$$\chi = \frac{D_\alpha - 1}{D_\gamma - 1} \tag{12}$$

The value of χ ranges from 0 to 1. A value approaching 0 indicates a highly heterogeneous distribution of BC and non-BC material among particles, whereas a value approaching 1 indicates that the BC-containing particles have similar BC-to-non-BC mass fractions. Thus, MR represents the overall amount of coating material, whereas χ describes how uniformly that material is distributed among BC-containing particles. Because only BC-containing particles were considered, χ represents the mixing uniformity within the BC-containing population rather than the mixing state of the entire aerosol population.

2.4 Models

2.4.1 The particle-resolved model PartMC-MOSAIC

PartMC-MOSAIC is a stochastic, particle-resolved aerosol model developed to simulate the evolution of aerosol size, chemical composition, and mixing state without imposing an a priori assumption of internal or external mixing (Riemer et al.,

https://doi.org/10.5194/egusphere-2026-5387
Preprint. Discussion started: 24 November 2026
© Author(s) 2026. CC BY 4.0 License.

2009; Zaveri et al., 2010). The model couples the Particle Monte Carlo model (PartMC) with the Model for Simulating Aerosol Interactions and Chemistry (MOSAIC) (Zaveri et al., 2008). In its box-model configuration, PartMC represents a well-mixed air parcel using an ensemble of computational particles.

Each computational particle is described by a composition vector,

$$\mu_i = (m_{i,s})_{s=1}^{S} \tag{13}$$

where $m_{i,s}$ represents the mass of chemical species s in particle i, and S is the total number of particle-phase species. This representation retains the compositional differences among individual particles and therefore provides a detailed description of aerosol mixing state.

PartMC simulates processes that change particle number and composition, including particle emissions, dilution, Brownian coagulation, deposition, and particle removal. These processes are generally represented as stochastic events using Monte Carlo methods. During coagulation, the composition vectors of two parent particles are combined to form a new particle, thereby conserving the mass of each chemical species. PartMC has been verified against analytical solutions and validated using aerosol chamber experiments (Tian et al., 2017; Shou et al., 2019).

MOSAIC provides deterministic calculations of gas-phase chemistry, aerosol thermodynamics, and dynamic gas–particle mass transfer. Its main components include the CBM-Z gas-phase chemical mechanism, the multicomponent Taylor expansion method for electrolyte activity coefficients, the multicomponent equilibrium solver for aerosols, and the adaptive step time-split Euler method for gas–particle partitioning (Zaveri et al., 2005a; Zaveri et al., 2005b; Zaveri et al., 2008). These modules describe the formation and partitioning of sulfate, nitrate, ammonium, chloride, aerosol water, and other relevant species.

Within the coupled framework, MOSAIC updates the chemical composition of individual particles through gas-phase reactions and gas – particle partitioning, while PartMC updates the particle population through emissions, coagulation, dilution, and removal. Assuming spherical particles and volume additivity, particle diameter, BC mass fraction, and coating thickness can be calculated from the composition of each particle. PartMC-MOSAIC is therefore well suited for investigating how BC mixing state evolves from relatively fresh, weakly coated particles towards more aged and internally mixed states.

The initial background aerosol population was constructed from the measured particle number size distribution and the joint distribution of total particle diameter (Dp) and BC-core diameter (D_c). BC-free particles were initialized using the measured non-BC particle number size distribution. For BC-containing particles, each valid $Dp - D_c$ combination was represented as a separate monodisperse mode, with its number concentration prescribed from the corresponding two-dimensional number distribution. BC-containing particles were represented as concentric core – shell structures. The non-BC material in both particle classes consisted of organic matter, sulfate, ammonium, nitrate, and chloride, accounting for 38.3 %, 25.7 %, 20.7 %, 9.3 %, and 6.0 % of the non-BC mass, respectively. Fresh particle emissions were represented by traffic and crop-residue-burning lognormal modes. The traffic mode contained 70 % BC and 30 % OC by dry mass, with a geometric

https://doi.org/10.5194/egusphere-2026-5387
Preprint. Discussion started: 24 November 2026
© Author(s) 2026. CC BY 4.0 License.

mean diameter (D_g) of 50 nm and a geometric standard deviation (σ_g) of 1.70 (Riemer et al., 2009; Zaveri et al., 2010). The crop-residue-burning mode contained 2.3 % BC, 43.1 % OC, 14.5 % chloride, and 40.1 % other inorganic material, with D_g = 120 nm and σ_g = 1.70, based on reported crop-residue-burning composition and biomass-burning particle size distributions (Janhäll et al., 2010; Ni et al., 2017). The prescribed mode strengths yielded traffic and crop-residue-burning contributions of approximately 72 % and 28 % to emitted BC mass. An emission scaling factor of 0.009 was defined as the baseline intensity. The environmental and temporal input parameters used in the baseline simulation are summarized in Table S1, while the gas-phase emission fluxes are listed in Table S2. The prescribed mixing-layer height, temperature, and pressure varied over the 6 d simulation following the observation-constrained time series shown in Fig. S1.

Each sensitivity simulation was conducted for 518400 s (6 d) using 100000 computational particles. The model integration time step was 60 s, and particle-resolved outputs were saved at 600 s intervals. One Monte Carlo realization was conducted for each single-process and process-free sensitivity simulation, whereas the all-process configuration was run with five independent random seeds to quantify stochastic variability. Across the five all-process realizations, the coefficients of variation in $D\alpha$, $D\gamma$, χ, σ_{abs}, and E_{abs} were all below 0.82 % (Fig. S2). The corresponding between-realization standard deviations represented only 0.7 %–2.2 % of the ranges among the six process configurations. These results indicate that stochastic variability was small relative to the process-induced differences under the present model configuration and was unlikely to alter the main conclusions. The first 86400 s (24 h) were treated as an initial adjustment period and excluded from the analysis to minimize the influence of transient adjustment to the prescribed initial aerosol and gas-phase conditions. Consequently, all results presented below were calculated from the remaining 432000 s (5 d) of each simulation. To evaluate the effects of individual atmospheric processes on the evolution of the BC mixing state, six sensitivity experiments were conducted, as summarized in Table 1.

Table 1. Configuration of the PartMC-MOSAIC sensitivity simulations used to isolate the effects of chemical processing, emissions, boundary-layer variation, and coagulation on BC mixing-state evolution. Check marks and crosses indicate whether the corresponding process was enabled or disabled, respectively.

Case	Chemical processing	Emissions	Boundary-layer variation	Coagulation
Case1	√	√	√	√
Case2	×	×	×	×
Case3	√	×	×	×
Case4	×	√	×	×
Case5	×	×	√	×
Case6	×	×	×	√

https://doi.org/10.5194/egusphere-2026-5387
Preprint. Discussion started: 24 November 2026
© Author(s) 2026. CC BY 4.0 License.

2.4.2 Particle-resolved Mie calculation of absorption coefficient and absorption enhancement

The absorption properties of BC-containing particles were calculated using a particle-resolved core-shell Mie model (Fierce et al., 2020; Yao et al., 2022; Zaveri et al., 2010). The component masses and number concentration represented by each computational particle were obtained from the PartMC-MOSAIC output. Component masses were converted to volumes using prescribed material densities. For each BC-containing particle i, the BC core diameter was calculated as

$$D_{\mathrm{c},i} = \left(\frac{6m_{\mathrm{BC},i}}{\pi\rho_{\mathrm{BC}}}\right)^{1/3} \tag{14}$$

where $m_{\mathrm{BC},i}$ is the BC mass of particle i. The prescribed densities of the individual aerosol components are listed in Table S3. The effective density of the non-BC material in each particle was calculated as

$$\rho_{\mathrm{other},i} = \frac{\sum_{j\neq\mathrm{BC}} m_{j,i}}{\sum_{j\neq\mathrm{BC}} m_{j,i}/\rho_j} \tag{15}$$

where the terms in the summations denote the mass and prescribed material density of each non-BC component. The total particle diameter was determined from the combined volumes of the BC core and non-BC coating:

$$D_{\mathrm{p},i} = \left[D_{\mathrm{c},i}^3 + \frac{6m_{\mathrm{other},i}}{\pi\rho_{\mathrm{other},i}}\right]^{1/3} \tag{16}$$

Each BC-containing particle was represented as a concentric sphere consisting of an absorbing BC core and a homogeneous non-BC shell. Calculations were performed at 880 nm using complex refractive indices of 1.67+0.67i for the BC core and 1.53+10^{-7}i (Tao et al., 2014; Zhao et al., 2021) for the non-BC coating. The absorption efficiency was calculated from the extinction and scattering efficiencies returned internally by the Mie solver:

$$Q_{\mathrm{abs},i} = Q_{\mathrm{ext},i} - Q_{\mathrm{sca},i} \tag{17}$$

The absorption cross section of each coated BC-containing particle was calculated as

$$C_{\mathrm{abs},i}^{\mathrm{coated}} = \pi\left(\frac{D_{\mathrm{p},i}}{2}\right)^2 Q_{\mathrm{abs},i}^{\mathrm{coated}} \tag{18}$$

The corresponding bare-BC absorption cross section was recalculated after removing the coating while retaining the same BC core mass, diameter, and refractive index:

$$C_{\mathrm{abs},i}^{\mathrm{bare}} = \pi\left(\frac{D_{\mathrm{c},i}}{2}\right)^2 Q_{\mathrm{abs},i}^{\mathrm{bare}} \tag{19}$$

The absorption coefficients of the coated and bare BC populations were obtained by weighting each single-particle absorption cross section by the number concentration represented by that computational particle:

https://doi.org/10.5194/egusphere-2026-5387
Preprint. Discussion started: 24 November 2026
© Author(s) 2026. CC BY 4.0 License.

$$\sigma_{\mathrm{abs}}^{\mathrm{coated}} = \sum_{i \in \mathrm{BC}} N_i \, C_{\mathrm{abs},i}^{\mathrm{coated}} \tag{20}$$

$$\sigma_{\mathrm{abs}}^{\mathrm{bare}} = \sum_{i \in \mathrm{BC}} N_i \, C_{\mathrm{abs},i}^{\mathrm{bare}} \tag{21}$$

where N_i is the number concentration represented by computational particle i.

The BC mass-normalized absorption coefficient was calculated as

$$\mathrm{MAC}_{\mathrm{BC}} = \frac{\sigma_{\mathrm{abs}}}{C_{\mathrm{BC}}} \tag{22}$$

where C_{BC} is the BC mass concentration.

For sensitivity analysis, E_{abs} was calculated using both the population-integrated ratio ($E_{\mathrm{abs}}^{\mathrm{pop}}$) and the arithmetic mean of particle-specific enhancement factors ($E_{\mathrm{abs}}^{\mathrm{arith}}$). Unless otherwise stated, the reported E_{abs} refers to $E_{\mathrm{abs}}^{\mathrm{pop}}$, which accounts for the unequal contributions of individual particles to population-level absorption. Retaining particle-to-particle heterogeneity is important because approaches based on population-mean coating properties may overestimate the bulk absorption enhancement of BC-containing aerosols (Yao et al., 2022; Fierce et al., 2020).

$$E_{\mathrm{abs}}^{\mathrm{pop}} = \frac{\sigma_{\mathrm{abs}}^{\mathrm{coated}}}{\sigma_{\mathrm{abs}}^{\mathrm{bare}}} = \frac{\sum_{i=1}^{N_{\mathrm{BC}}} w_i \, C_{\mathrm{abs},i}^{\mathrm{coated}}}{\sum_{i=1}^{N_{\mathrm{BC}}} w_i \, C_{\mathrm{abs},i}^{\mathrm{bare}}} \tag{23}$$

$$E_{\mathrm{abs}}^{\mathrm{arith}} = \frac{1}{N_{\mathrm{BC}}} \sum_{i=1}^{N_{\mathrm{BC}}} \frac{C_{\mathrm{abs},i}^{\mathrm{coated}}}{C_{\mathrm{abs},i}^{\mathrm{bare}}} \tag{24}$$

3 Results and discussion

3.1 Overview of the field observations

Figure 2 shows the temporal evolution of the meteorological conditions, aerosol optical properties, BC characteristics, mixing-state parameters, and PNSD during the campaign. From 26 May to 18 June 2018, generally weak winds prevailed, with a mean WS of 1.9 ± 1.0 m s^{-1} and a median of 1.8 m s^{-1}. Approximately 59 % and 84 % of the observations had WS below 2 and 3 m s^{-1}, respectively, indicating generally limited near-surface ventilation. E, SE, and S winds accounted for 27.6 %, 19.9 %, and 18.1 % of the observations, respectively, together representing approximately 66 % of the campaign, indicating the predominance of easterly and southerly airflow. Given the location of Taizhou between Nanjing and Shanghai, these airflows may have transported a mixture of regional anthropogenic emissions and maritime air masses to the observation site (Ma et al., 2022).

The campaign-average T and RH were 24 ± 4 °C and 71 ± 18 %, respectively. Both variables exhibited pronounced and opposing diurnal variations, with higher T and lower RH during daytime and more humid conditions at night and in the early morning. The combination of warm daytime conditions and humid nighttime conditions is favourable for investigating different pathways of aerosol processing. Daytime photochemistry can produce condensable secondary material, whereas

https://doi.org/10.5194/egusphere-2026-5387
Preprint. Discussion started: 24 November 2026
© Author(s) 2026. CC BY 4.0 License.

elevated RH can promote hygroscopic growth, heterogeneous reactions, and gas-to-particle partitioning. Previous measurements in the YRD showed that increasing RH from 40 % to 85 % enhanced aerosol scattering by approximately 58 %, illustrating the importance of humidification for aerosol optical properties in this region (Zhang et al., 2015).

Considerable variability was observed in the aerosol loading and optical properties. The campaign-average σ_{sca} and σ_{abs} were 142.65 ± 99.22 and 12.07 ± 10.00 Mm^{-1}, respectively. Their large relative standard deviations, together with the pronounced peaks in Fig. 2, indicate repeated transitions between relatively clean and polluted conditions. The mean BC mass concentration was 1.43 ± 1.04 $\mu g\, m^{-3}$. This value was lower than the annual mean of 2.3 $\mu g\, m^{-3}$reported for urban Shanghai, where BC concentrations were also shown to depend strongly on WS and regional transport (Zha et al., 2014). It was also lower than the 2.80 – 3.65 $\mu g\, m^{-3}$ observed during wintertime in urban Nanjing (Li et al., 2020). These differences are consistent with the suburban character and warm-season timing of the Taizhou campaign.

The campaign-mean value of the time-resolved median particle diameter was 85 ± 28 nm, with individual median values ranging from approximately 21 to 159 nm. Periods dominated by Aitken-mode particles alternated with periods of enhanced accumulation-mode particles, possibly reflecting changes in the relative contributions of new particle formation, primary emissions, condensational growth, coagulation, and regional transport.

The mean MR, χ, D_α, and D_γ were 2.63 ± 0.62, 0.728 ± 0.031, 1.539 ± 0.057, and 1.739 ± 0.059, respectively. The moderate MR indicates that BC cores were generally associated with appreciable amounts of non-BC material, while the relatively narrow range of χ suggests that the degree of particle-to-particle mixing heterogeneity was more stable than the bulk coating amount. Atmospheric aging experiments have shown that BC particles can grow rapidly through the condensation of secondary material, with substantial changes in particle morphology and optical properties occurring within several hours (Peng et al., 2017). Moreover, field observations and particle-resolved optical calculations have demonstrated that BC absorption enhancement cannot be determined solely from the bulk non-BC-to-BC mass ratio because the distribution of coating material among individual particles also plays a critical role (Zhai et al., 2022).

Overall, the coexistence of limited near-surface ventilation, variable RH, changing air-mass origins, substantial PNSD variability, and repeated clean-to-polluted transitions provides a useful natural framework for investigating BC aging and mixing-state evolution. These conditions enable the responses of MR, χ, D_α, and D_γ to be evaluated under contrasting aerosol loadings and characteristic particle sizes, thereby helping to distinguish the effects of bulk coating amount from particle-to-particle heterogeneity and to improve the interpretation of BC optical properties under atmospherically relevant conditions.

https://doi.org/10.5194/egusphere-2026-5387
Preprint. Discussion started: 24 November 2026
© Author(s) 2026. CC BY 4.0 License.

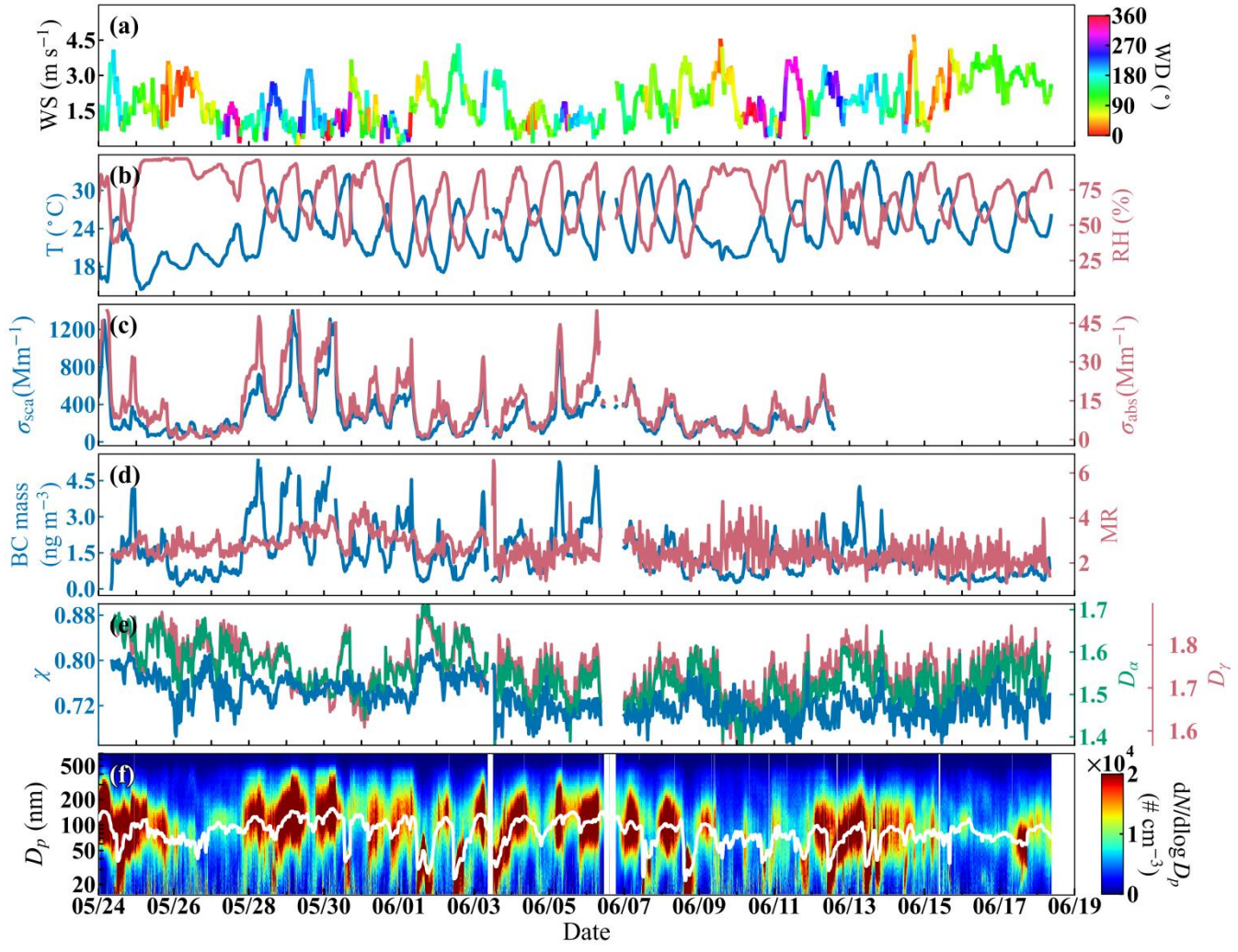

Figure 2: Time series of (a) WS and WD; (b) T and RH; (c) σ_{sca} and σ_{abs}; (d) BC mass concentration and MR; (e) χ, D_α, and D_γ; and (f) PNSD as a function of D_p. The overlaid curve in (f) represents the smoothed median D_p, and the scale denotes $dN/d\log D_p$.

3.2 Observed diurnal variations in the BC mixing state and related properties

3.2.1 Campaign-mean diurnal variations in meteorological conditions and key aerosol properties

Figure 3 presents the diurnal variations in meteorological conditions, BC mixing-state parameters, and aerosol absorption properties during the campaign. T and RH exhibited pronounced opposite cycles. T decreased to approximately 20 °C before sunrise, increased rapidly during the morning, and reached about 29 °C in the afternoon. In contrast, RH increased to approximately 90 % in the early morning, decreased to around 50 % in the afternoon, and subsequently recovered during the evening. These variations reflect the combined effects of surface heating and boundary-layer development.

https://doi.org/10.5194/egusphere-2026-5387
Preprint. Discussion started: 24 November 2026
© Author(s) 2026. CC BY 4.0 License.

MR was highest at approximately 03:00–04:00 and generally decreased during the daytime. The coincidence of high MR with low T and high RH suggests that cool and humid conditions favoured the partitioning and accumulation of non-BC material on BC-containing particles. In contrast, daytime heating may have promoted the evaporation of nitrate and semi-volatile organic material, while boundary-layer development enhanced atmospheric dilution. The continuous input of freshly emitted and weakly coated BC may also have contributed to the daytime decrease in MR.

Both D_α and D_γ were relatively low during the daytime and increased markedly after approximately 16:00. However, χ exhibited a distinct pattern, remaining relatively low and variable around noon before increasing rapidly in the evening. This difference arises because MR represents the bulk amount of non-BC material relative to BC, whereas χ describes how uniformly that material is distributed among BC-containing particles. Therefore, variations in the bulk coating amount or particle diversity do not necessarily lead to a corresponding change in χ.

Previous observations in Beijing and Xianghe showed that internally mixed or thickly coated BC reached a maximum around noon because of enhanced photochemical aging (Cheng et al., 2012; Zhang et al., 2018). In contrast, no clear midday increase in χ was observed at Taizhou. Zhao et al. (2021) using measurements from the same campaign, similarly reported lower daytime χ and attributed it to the mixing of freshly emitted, weakly coated BC with pre-existing aged particles. Although daytime photochemistry produced condensable secondary material, its homogenizing effect may have been offset by fresh BC emissions, volatilization of semi-volatile coatings, and boundary-layer mixing of particles from different sources and aging stages.

After the late afternoon, decreasing T and increasing RH were consistent with enhanced aerosol liquid-water uptake and provided favourable conditions for nocturnal aqueous and heterogeneous reactions. During the same field campaign in Taizhou, Wang et al. (2020) observed rapid nighttime loss and uptake of N_2O_5, indicating efficient heterogeneous hydrolysis and particulate nitrate formation. Li et al. (2018) also found that nighttime nitrate formation under cool and humid conditions substantially altered the coating and mixing state of BC particles. Secondary nitrate and other products formed through aerosol liquid-phase processing may have been distributed across a broad fraction of the BC-containing population, reducing particle-to-particle compositional differences and increasing χ during the evening.

The absorption coefficient exhibited a pronounced morning maximum and an afternoon minimum, likely reflecting the combined influences of morning emissions, BC accumulation within a shallow boundary layer, and enhanced daytime dilution. The BC mass-normalized absorption coefficient displayed a different diurnal pattern and did not vary consistently with χ. In particular, the morning absorption maximum coincided with relatively low χ, whereas the evening increase in χ was not accompanied by a comparable increase in absorption. These results suggest that the observed absorption variations were influenced jointly by BC loading, coating amount, particle-to-particle heterogeneity, particle size, and coating composition.

https://doi.org/10.5194/egusphere-2026-5387
Preprint. Discussion started: 24 November 2026
© Author(s) 2026. CC BY 4.0 License.

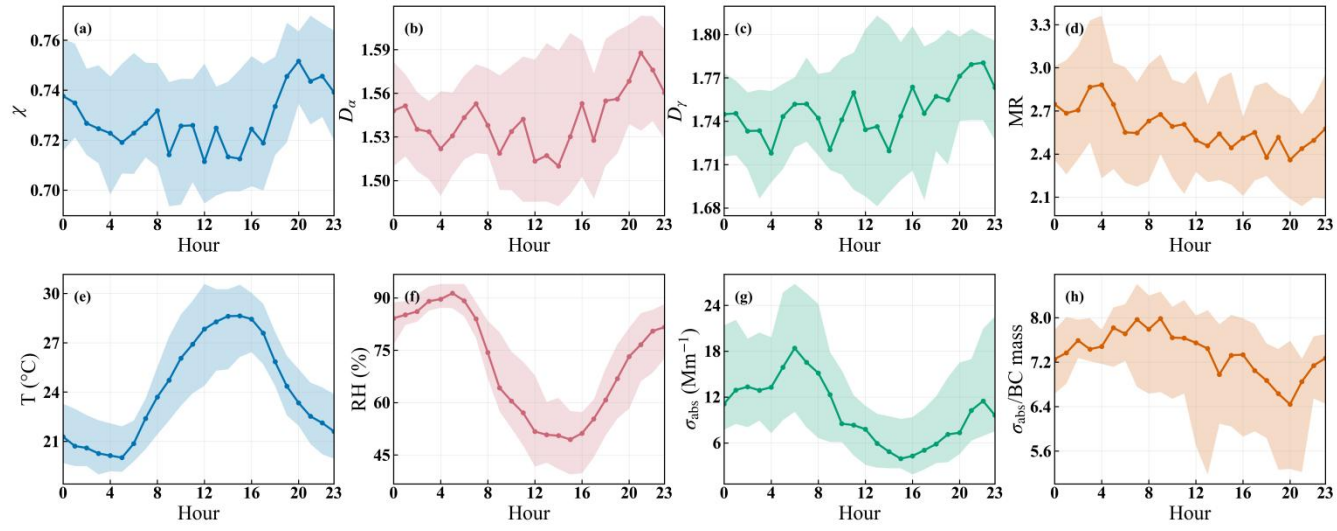

Figure 3: Diurnal variations in (a) χ, (b) D_α, (c) D_γ, (d) MR, (e) T, (f) RH, (g) the σ_{abs}, and (h) the BC mass-normalized absorption coefficient during the campaign. Solid lines and shaded areas represent the hourly medians and interquartile ranges, respectively.

3.2.2 Diurnal trajectories of the BC mixing state in Dα–Dγ space

Figure 4 presents the hourly trajectories of the BC mixing state in Dα–Dγ space for the campaign mean and for 1, 4, and 8 June 2018. The campaign-mean trajectory exhibited three stages: relatively low D_α, D_γ, and χ during the daytime, a simultaneous increase after approximately 16:00, and a subsequent decline from the evening maxima after approximately 20:00. The low daytime metrics do not imply weak photochemistry. Measurements during the same Taizhou campaign demonstrated strong daytime atmospheric oxidation capacity capable of continuously producing oxidized and condensable secondary material (Ma et al., 2022). However, primary emissions introduce weakly coated BC, while boundary-layer development, air-mass exchange, and loss of semi-volatile coatings modify the relative contributions of particles with different coating states. The low daytime mixing-state metrics therefore more likely represent the net outcome of competition between secondary coating formation and heterogenizing processes associated with primary emissions and atmospheric mixing, rather than the response to photochemical aging alone (Lee et al., 2019; Tao et al., 2024). Hourly wind speed, wind direction, and other meteorological variables for the three representative days are shown in Figs. S3–S5.

After approximately 16:00, decreasing temperature and increasing RH coincided with marked increases in D_α, D_γ, and χ, whereas MR showed no increase of comparable magnitude. This indicates that the evening evolution was not driven primarily by a substantial increase in the bulk non-BC coating amount, but instead reflected convergence in the BC–non-BC mass fractions of individual particles. Semi-volatile oxidation products generated during the daytime may have repartitioned into the particle phase as the atmosphere cooled, while elevated RH and aerosol water favoured nocturnal gas–particle partitioning and heterogeneous chemistry. Measurements during the same campaign showed rapid nighttime N_2O_5 loss and

https://doi.org/10.5194/egusphere-2026-5387
Preprint. Discussion started: 24 November 2026
© Author(s) 2026. CC BY 4.0 License.

particle uptake, providing direct evidence for nocturnal particulate nitrate formation, and recent direct measurements have demonstrated that aerosol water can substantially promote N_2O_5 uptake (Wang et al., 2020; Li et al., 2025). These processes may have modified the compositions of a broader fraction of BC-containing particles, thereby reducing particle-to-particle differences and increasing χ without requiring a comparable increase in MR.

The decline in the mixing-state metrics after approximately 20:00 indicates that humid conditions did not necessarily produce continuous population-wide homogenization. One possible mechanism is that, as humid processing persisted, larger, more hygroscopic, or more strongly coated accumulation-mode particles retained more aerosol water and provided greater reactive surface area and condensation sink. Subsequent secondary material may therefore have been taken up preferentially by these particles, whereas smaller or weakly coated BC particles underwent more limited compositional changes. The contrast between thickly and weakly coated particles could consequently increase again, causing χ to decline. This explanation should be regarded as a mechanism consistent with the observations rather than as direct proof, because nighttime emissions or changes in air-mass origin could produce a similar response. Recent single-particle observations also demonstrate that substantial coating and compositional variability can persist even when population-mean aerosol properties are similar (Farley et al., 2024).

The three representative days shared a nighttime decline but differed substantially in the strength of their daytime-to-evening recovery. On 1 and 8 June, enhancements of sub-100 nm particles coincided with marked increases in D_α, D_γ, and χ. This coordinated evolution is consistent with enhanced condensational processing, which may have redistributed non-BC material among BC-containing particles and thereby increased both their compositional diversity and mixing uniformity (Lee et al., 2019). The small-particle mode was stronger and the afternoon BC loading was lower on 8 June, allowing a similar amount of non-BC material to produce a larger change in BC-non-BC mass fractions. In contrast, the weaker sub-100 nm enhancement and persistent accumulation mode on 4 June may indicate either a more limited condensable-material supply or preferential uptake by pre-existing larger particles, resulting in recovery of the bulk composition but weaker particle-level homogenization. Because emissions, chemical aging, boundary-layer evolution, and coagulation occurred simultaneously, the following section uses observation-constrained PartMC-MOSAIC sensitivity simulations to isolate their respective effects on D_α, D_γ, and χ (Zhang et al., 2025).

https://doi.org/10.5194/egusphere-2026-5387
Preprint. Discussion started: 24 November 2026
© Author(s) 2026. CC BY 4.0 License.

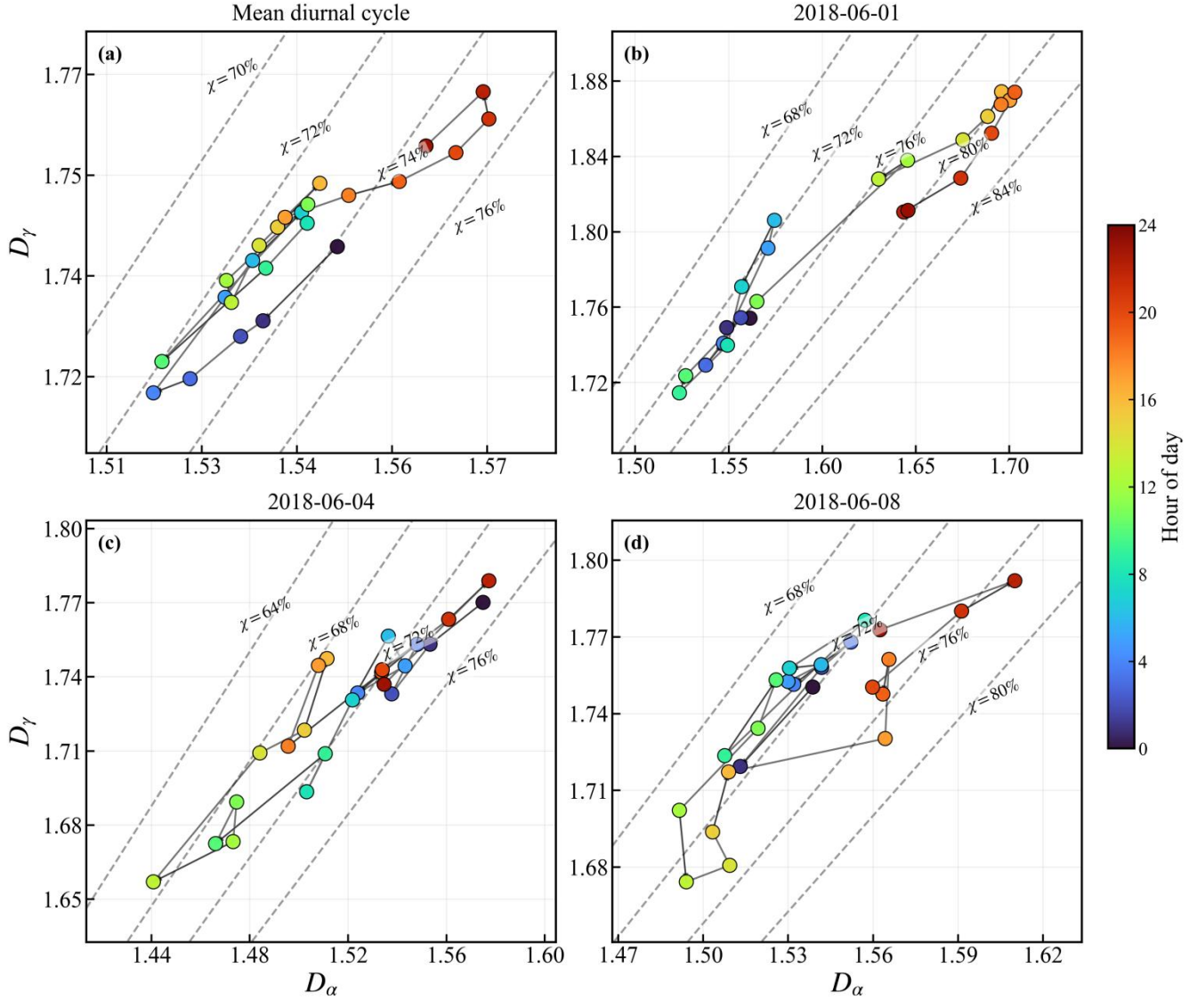

Figure 4: Diurnal evolution of the BC mixing state in Dα-Dγ space.

3.3 Simulated evolution of the BC mixing state using PartMC-MOSAIC

3.3.1 Effects of individual atmospheric processes on the BC mixing-state index

Figure 5 compares the temporal evolution, mean diurnal cycles, and statistical distributions of the BC mixing-state index among the six sensitivity simulations. In Case 2, χ remained at 0.79 throughout the simulation. Chemical aging produced the highest mean χ of 0.89 ± 0.01, 11.9 % above Case 2. This increase is consistent with the formation and partitioning of secondary material reducing differences in the BC and non-BC mass fractions among individual particles. By contrast, fresh emissions decreased the mean χ to 0.53 ± 0.07, 32.6 % below Case 2. The progressive decline indicates that the

https://doi.org/10.5194/egusphere-2026-5387
Preprint. Discussion started: 24 November 2026
© Author(s) 2026. CC BY 4.0 License.

continuous introduction of BC-rich particles compositionally distinct from the aged background increased particle-to-particle heterogeneity. Such contrasting responses are consistent with previous particle-resolved studies showing that condensation-driven aging tends to homogenize particle compositions, whereas fresh emissions can maintain or enhance population heterogeneity (Lee et al., 2019; Zhao et al., 2021).

With all processes included, Case 1 yielded a mean χ of 0.74 $\pm$ 0.03. Its non-monotonic evolution reflects the combined and temporally varying influences of fresh particle input, chemical aging, boundary-layer variation, and coagulation. Cases 5 and 6 showed negligible changes in χ and remained close to Case 2 throughout the simulation. Thus, under the simulated conditions, chemical aging and fresh emissions produced the largest, but opposite, changes in χ, whereas boundary-layer variation and coagulation had limited effects on its mean value. Their different effects become clearer when D_α and D_γ are considered separately in Sect. 3.3.2.

https://doi.org/10.5194/egusphere-2026-5387
Preprint. Discussion started: 24 November 2026
© Author(s) 2026. CC BY 4.0 License.

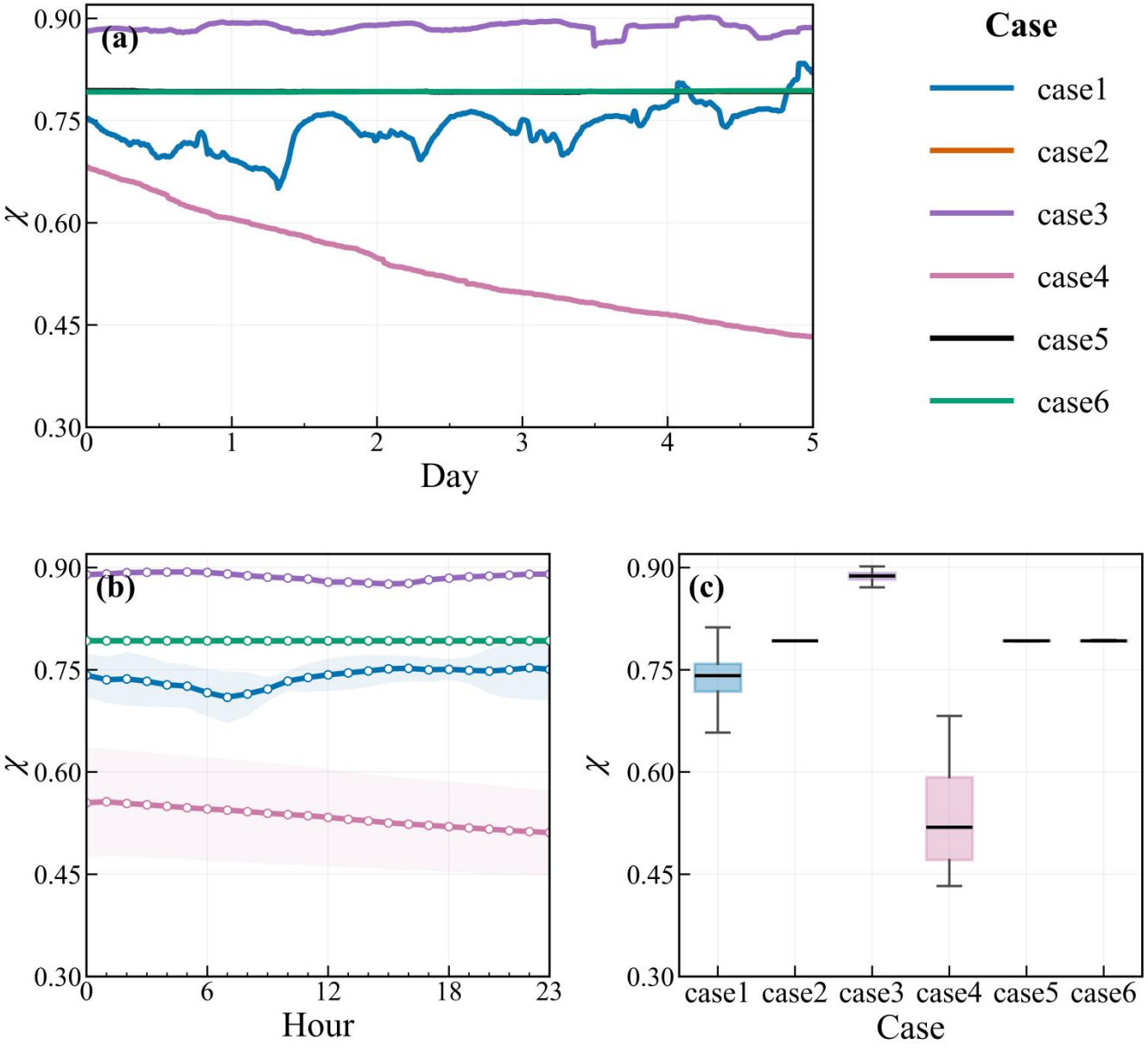

Figure 5: Process-dependent evolution and diurnal variability of the BC mixing-state index (χ) in the PartMC-MOSAIC sensitivity simulations. (a) Five-day time series; (b) mean diurnal cycles; and (c) case-wise statistical distributions.

3.3.2 Process-dependent evolution of D_α, D_γ, and χ

Figure 6 shows the daily trajectories of the BC-containing particle populations from Day 1 (D1) to Day 5 (D5) in D_α–D_γ space. Case 2 remained fixed at D_α=1.53, D_γ=1.68, and χ=0.79, providing a reference for evaluating process-induced changes. Case 5 showed little displacement. Case 4 followed a pronounced upper-left trajectory: D_α decreased from 1.50 to

https://doi.org/10.5194/egusphere-2026-5387
Preprint. Discussion started: 24 November 2026
© Author(s) 2026. CC BY 4.0 License.

1.41, whereas D_γ increased from 1.77 to 1.93 and χ decreased from 0.64 to 0.45. These changes indicate lower mean compositional diversity within individual particles but greater compositional diversity across the population. This response is consistent with compositionally simple, BC-rich particles being introduced into an aged background population, thereby increasing particle-to-particle heterogeneity (O'brien et al., 2015; Wu et al., 2024).

Case 3 followed a contrasting upper-right trajectory. From D1 to D5, D_α increased from 1.21 to 1.32 and D_γ from 1.24 to 1.36, while χ remained close to 0.89. The concurrent increases in the two diversity parameters suggest that secondary-material formation and gas–particle partitioning increased both particle-level and population-level compositional diversity (Riemer and West, 2013; Bondy et al., 2018). By contrast, Case 6 followed a lower-left trajectory: D_α decreased from 1.50 to 1.43 and D_γ from 1.63 to 1.54, while χ remained close to 0.79. Thus, coagulation reorganized particle composition within the BC-containing population without producing a comparable change in the normalized mixing-state index (Shou et al., 2019). To further elucidate the differences between the two processes, Fig. S6 compares the size and coating properties of BC-containing particles. Chemical aging increased the median MR from 10.98 to 12.22, while D_p/D_c decreased from 2.82 to 2.50. This divergence indicates that changes in dry coating composition did not translate directly into geometric particle growth, partly because MR excludes water whereas D_p includes particle water and is affected by volatile partitioning. In contrast, coagulation increased the median MR from 3.45 to 4.93 and D_p/D_c from 1.72 to 1.90. Chemical aging was therefore associated primarily with secondary-material addition and redistribution among existing particles, whereas coagulation reorganized existing BC and non-BC mass through particle merging. These distinct mechanisms help explain their contrasting trajectories in D_α–D_γ space.

Case 1 exhibited a non-monotonic trajectory reflecting the combined effects of the simulated processes. Both D_α and D_γ increased from 1.27 and 1.38 on D1 to 1.49 and 1.66 on D4, respectively, before decreasing to 1.46 and 1.59 on D5; over the same period, χ increased from 0.72 to 0.78. The initial increase indicates greater particle-level and population-level diversity, whereas the subsequent reversal suggests a shift in the relative contributions of the simultaneously operating processes. Importantly, Cases 2, 5, and 6 yielded similar χ values despite occupying different positions or following different trajectories in D_α–D_γ space. Joint analysis of D_α, D_γ, and χ therefore provides process-related information that cannot be obtained from χ alone.

https://doi.org/10.5194/egusphere-2026-5387
Preprint. Discussion started: 24 November 2026
© Author(s) 2026. CC BY 4.0 License.

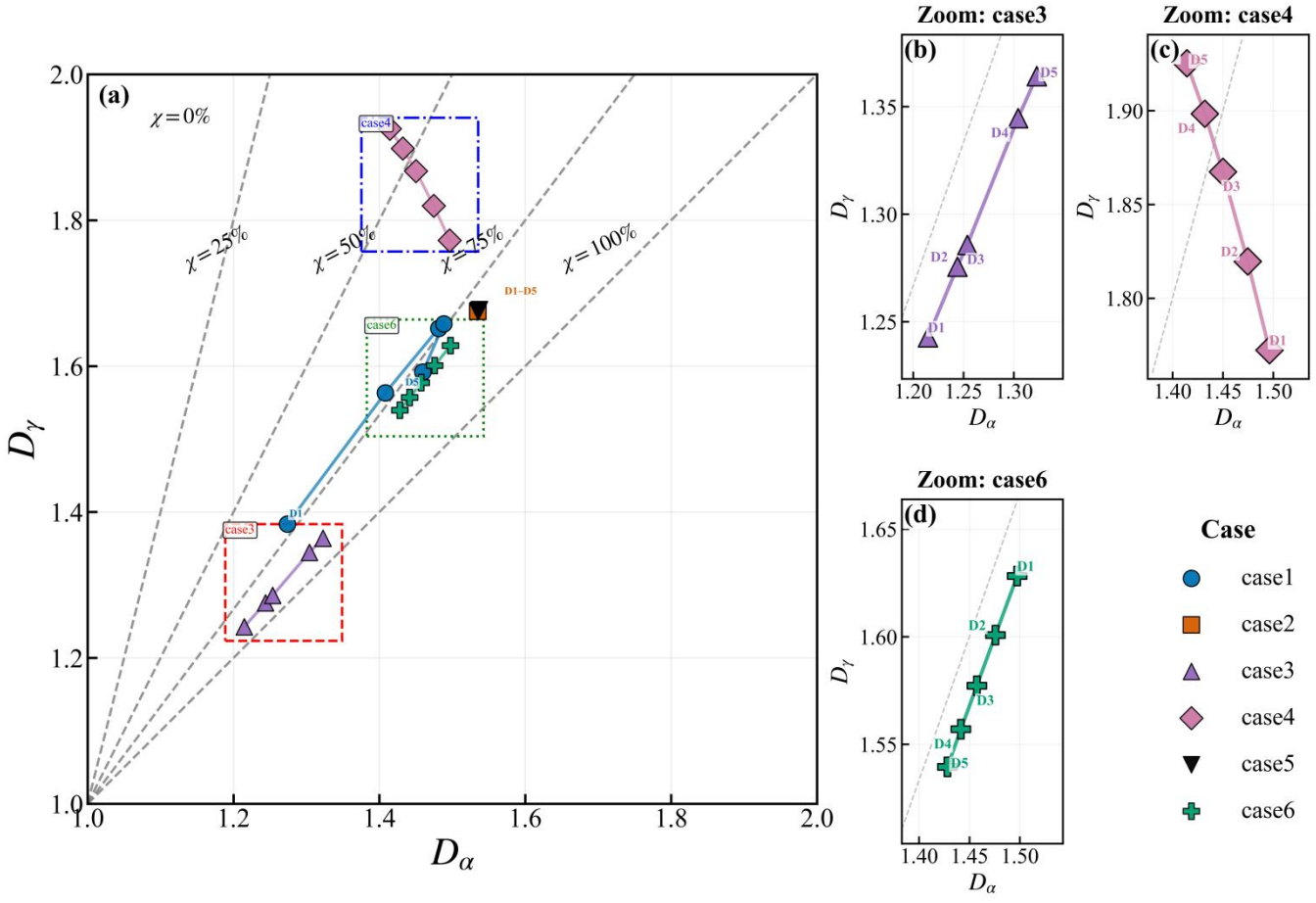

Figure 6: Process-dependent daily trajectories of the simulated particle populations in D_α–D_γ space.

3.4 Optical effects of BC mixing-state evolution

3.4.1 Process-dependent changes in the BC absorption coefficient

Figure 7 compares the temporal evolution, mean diurnal cycles, and statistical distributions of the σ_{abs} among the six sensitivity simulations. Case 2 served as the process-free reference and had a mean σ_{abs} of 6.07 ± 0.08 Mm^{-1}. Case 4 produced the highest mean value of 9.01 ± 1.21 Mm^{-1}, 48.4 % above Case 2. Its progressive increase is consistent with the accumulation of newly emitted BC during the simulation. As a population-integrated quantity, σ_{abs} is influenced by both BC loading and particle-specific absorption efficiency. The response in Case 4 is therefore consistent with the close relationship between BC mass and absorption reported in previous studies (Bond and Bergstrom, 2006; Liu et al., 2023). Case 3 also showed a substantial increase, reaching 7.79 ± 0.53 Mm^{-1}, 28.3 % above Case 2, despite the absence of additional BC emissions. This response is consistent with secondary coating formation increasing the calculated absorption cross sections of BC-containing particles through the lensing effect represented by the core–shell model (Shiraiwa et al., 2007; Shiraiwa et

https://doi.org/10.5194/egusphere-2026-5387
Preprint. Discussion started: 24 November 2026
© Author(s) 2026. CC BY 4.0 License.

al., 2008; Xu et al., 2018). Case 1 produced a comparable mean of 7.68 ± 0.68 Mm^{-1}, but its morning maximum, afternoon minimum, and evening recovery suggest a combined response to emissions, chemical processing, dilution, and particle redistribution.

Case 5 produced only a small increase, with a mean σ_{abs} of 6.17 ± 0.07 Mm^{-1}, 1.7 % above Case 2. This limited response suggests that the prescribed boundary-layer variation had little net influence on absorption under the present box-model configuration. Case 6 increased the mean to 6.40 ± 0.09 Mm^{-1}, 5.4 % above Case 2. Because coagulation conserves BC mass, this modest increase is consistent with changes in particle size and the redistribution of BC and non-BC material, which can alter the population-integrated absorption cross section. Observations have similarly demonstrated the sensitivity of bulk absorption to the BC size distribution (Zhao et al., 2023). The mean ordering was Case 4 > Case 3 > Case 1 > Case 6 > Case 5 > Case 2. Under the present model configuration, this ordering suggests that emissions produced the largest change in σ_{abs} through additional BC loading, while chemical aging provided a substantial coating-related enhancement; boundary-layer variation and coagulation produced smaller responses.

https://doi.org/10.5194/egusphere-2026-5387
Preprint. Discussion started: 24 November 2026
© Author(s) 2026. CC BY 4.0 License.

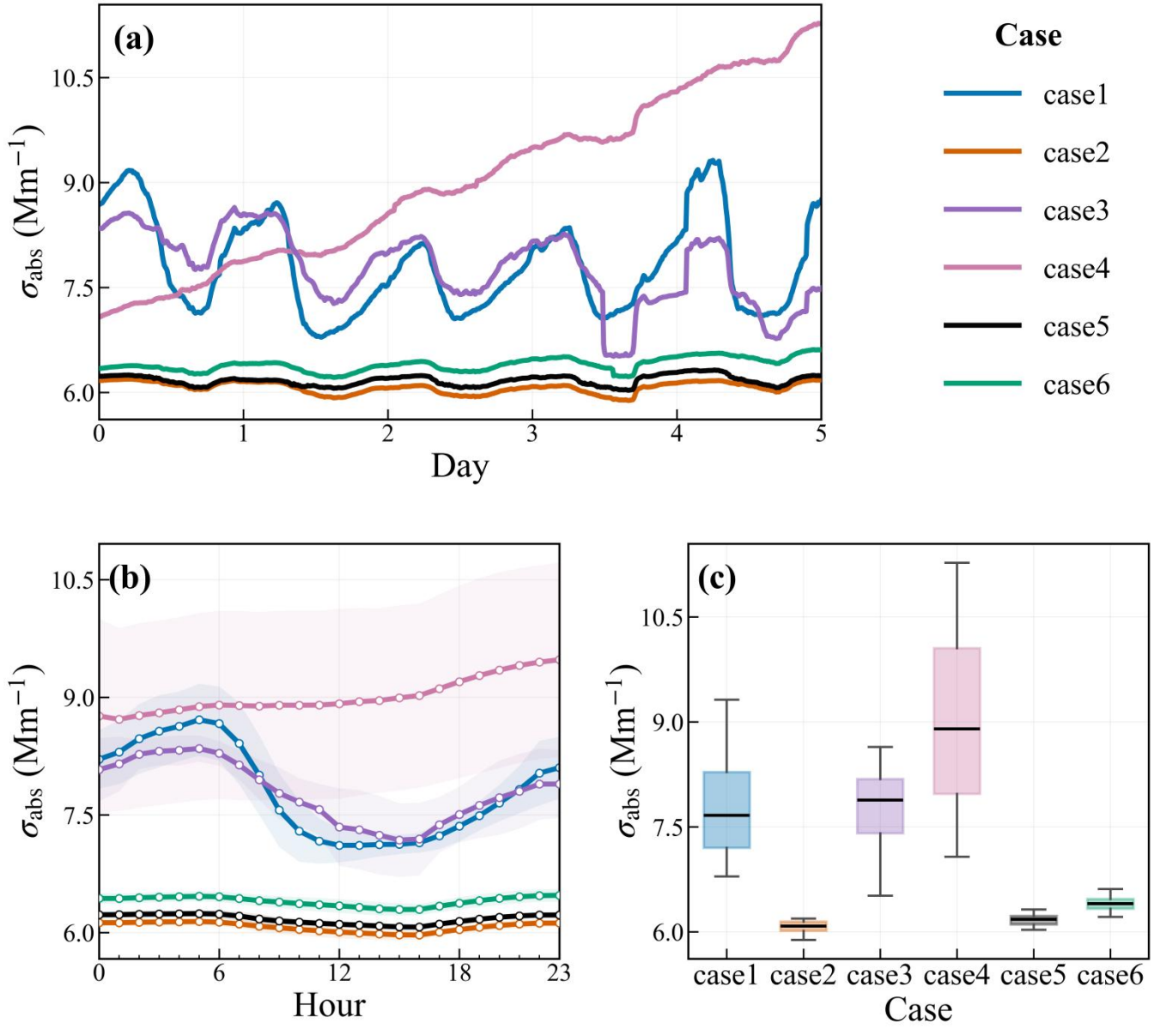

Figure 7: Process-dependent evolution and diurnal variability of the BC absorption coefficient (σabs) in the PartMC-MOSAIC sensitivity simulations. (a) Five-day time series; (b) mean diurnal cycles; and (c) case-wise statistical distributions.

3.4.2 Process-dependent changes in BC absorption enhancement

Figure 8 shows the variation in BC absorption enhancement among the sensitivity simulations. Case 2 served as the process-free reference, with E_{abs} remaining nearly constant at 1.46 throughout the simulation. Case 3 produced the largest enhancement, with a mean of 1.85 ± 0.11, 27.1 % above Case 2. Its morning maximum and afternoon minimum are consistent with diurnal changes in the coating-to-core ratio. Within the adopted core – shell representation of the Mie

https://doi.org/10.5194/egusphere-2026-5387
Preprint. Discussion started: 24 November 2026
© Author(s) 2026. CC BY 4.0 License.

scattering model, the partitioning of secondary material enlarged the non-BC shell and increased the calculated lensing effect. Laboratory and field studies have similarly associated chemical aging and coating growth with enhanced BC absorption, although the magnitude depends on particle morphology and coating properties (Peng et al., 2016; Yuan et al., 2020; Wei et al., 2024). By contrast, Case 4 produced the lowest mean E_{abs} of 1.28 ± 0.05, 12.2 % below Case 2. Its gradual decline is consistent with an increasing contribution from freshly emitted, weakly coated BC particles. This interpretation is further supported by the emission-gradient simulations (Fig. S7). The absorption coefficient increased approximately linearly with the emission multiplier F ($\sigma_{abs} = 6.148 + 2.798$ F, $R^2 = 0.998$), whereas χ and E_{abs} decreased approximately logarithmically ($\chi = 0.530 - 0.131$ ln F, $R^2 = 0.991$); ($E_{abs} = 1.275 - 0.089$ ln F, $R^2 = 0.991$). Doubling F therefore corresponded to approximate decreases of 0.09 in χ and 0.06 in E_{abs}. Together with the highest σ_{abs} in Case 4 (Sect. 3.4.1), these results suggest that increasing fresh emissions enhanced bulk absorption mainly through additional BC mass while increasing particle-to-particle heterogeneity and reducing coating-induced enhancement. Case 1 showed an intermediate and more variable response, with a mean E_{abs} of 1.50 ± 0.10, likely reflecting competition between coating formation and changes in the relative abundance of particles with different coating states.

Case 5 remained close to Case 2, with a mean E_{abs} of 1.45 and a relative difference of only 0.1 %. This small response suggests that concentration changes had little effect on the enhancement ratio when particle composition was largely unchanged. Case 6 increased E_{abs} to 1.52 ± 0.02, 4.4 % above Case 2. Because coagulation conserves BC mass, this modest enhancement is consistent with the redistribution of BC and non-BC material among particles, which altered their effective coating-to-core ratios and modelled optical geometry. The mean ordering was Case 3 > Case 6 > Case 1 > Case 2 ≈ Case 5 > Case 4. Under the present model configuration, this ordering indicates that E_{abs} was more responsive to process-induced changes in coating amount and its particle-to-particle distribution than to changes in BC abundance alone. Coupled-process simulations showed that the responses of χ, σ_{abs}, and E_{abs} were not fully additive (Fig. S8). Interactions involving boundary-layer variation were generally stronger, whereas the four-process interaction was comparatively small. The particle arithmetic mean exceeded the population-integrated E_{abs} by 11.4 % – 26.5 % across the simulations (Fig. S9). The case-dependent differences demonstrate that the calculated enhancement is sensitive to the particle-to-particle distribution of absorption contributions.

https://doi.org/10.5194/egusphere-2026-5387
Preprint. Discussion started: 24 November 2026
© Author(s) 2026. CC BY 4.0 License.

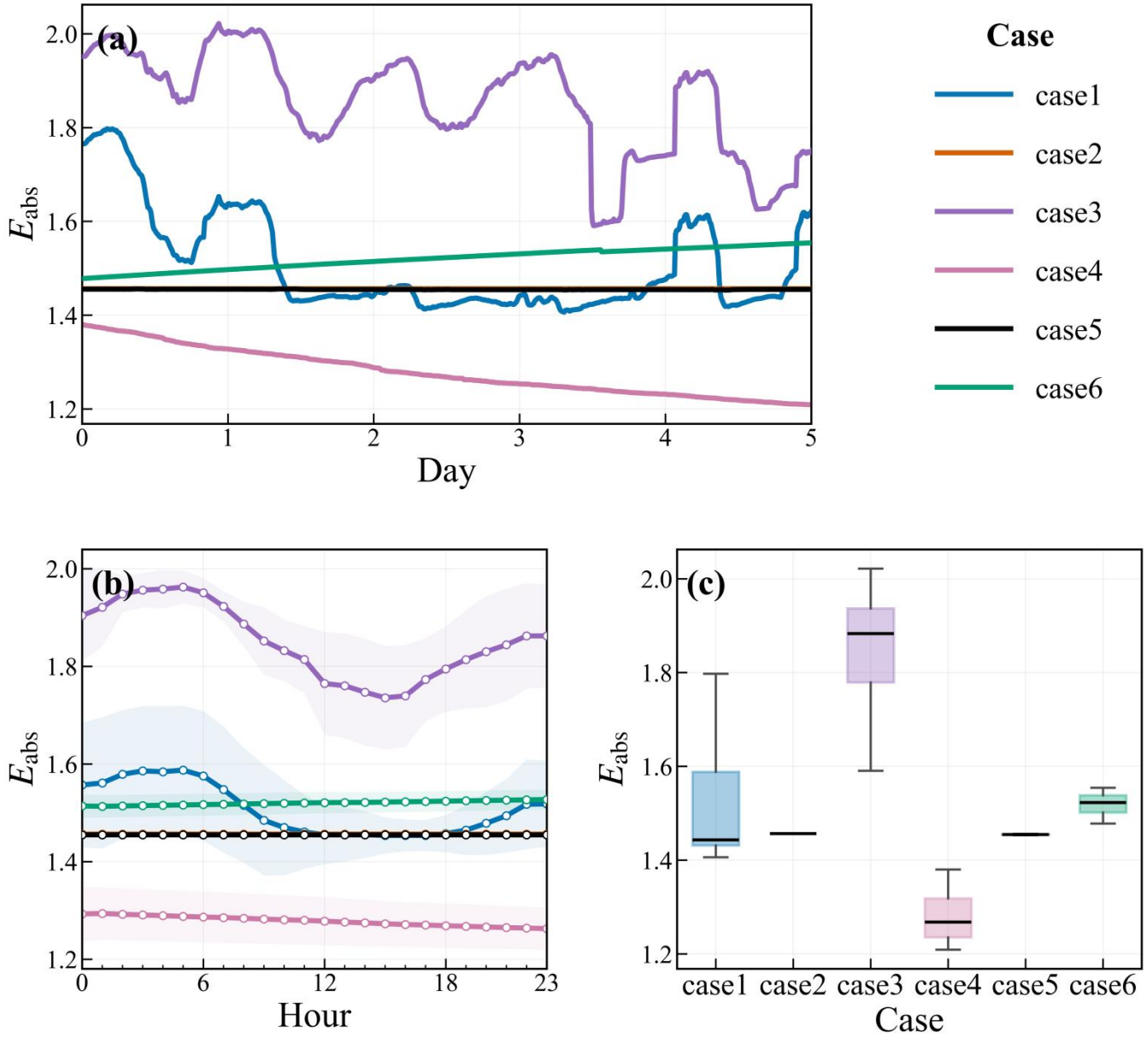

Figure 8: Process-dependent evolution and diurnal variability of BC absorption enhancement (E_{abs}) in the PartMC-MOSAIC sensitivity simulations. (a) Five-day time series; (b) mean diurnal cycles; and (c) case-wise statistical distributions.

4 Conclusion

This study combined size-resolved measurements of BC core and coating properties in suburban Taizhou with observation-constrained PartMC-MOSAIC simulations and a core – shell representation of the Mie scattering model to investigate the coupled evolution of BC heterogeneity and optical absorption. The observed BC-containing particle

https://doi.org/10.5194/egusphere-2026-5387
Preprint. Discussion started: 24 November 2026
© Author(s) 2026. CC BY 4.0 License.

population was characterized by appreciable coating and incomplete internal mixing. The three diversity metrics remained relatively low during the daytime, increased markedly in the late afternoon, and subsequently declined during the evening. In contrast, MR did not exhibit a comparable evening increase. This decoupling is consistent with a redistribution of non-BC material among BC-containing particles rather than a simple increase in bulk coating amount, suggesting that population-mean coating metrics alone cannot fully characterize the evolution of BC mixing state.

The sensitivity simulations showed that chemical aging and fresh emissions exerted the largest but opposite effects on BC heterogeneity under the simulated conditions. Chemical aging increased χ, whereas fresh emissions decreased it markedly. Boundary-layer variation and coagulation produced comparatively small changes in the mean χ. However, the trajectories in D_α–D_γ space revealed process-dependent changes that were not apparent from χ alone. Chemical aging increased both particle-level and population-level diversity, whereas fresh emissions decreased particle-level diversity but increased population-level diversity. Coagulation reduced both diversity parameters while producing little net change in χ. Similar mixing-state indices can therefore represent particle populations with different compositional structures and atmospheric histories. Joint analysis of $D\alpha$, $D\gamma$, and χ provides a more informative basis for distinguishing the effects of atmospheric processes on BC heterogeneity.

Fresh emissions produced the largest increase in σ_{abs} while decreasing E_{abs}, suggesting that their effect on bulk absorption was mainly associated with additional BC loading rather than stronger coating-induced enhancement. Chemical aging increased both σ_{abs} and E_{abs}, consistent with the growth of non-BC coatings and the resulting increase in the calculated lensing effect. Coagulation produced a comparatively modest change in bulk absorption but yielded the second-highest mean E_{abs}, reflecting the reorganization of particle size and composition and the redistribution of non-BC material among BC-containing particles. Boundary-layer variation had relatively little influence on E_{abs}. Overall, under the present model configuration, σ_{abs} was more closely associated with changes in BC loading, whereas E_{abs} responded more strongly to coating evolution and its particle-to-particle distribution. Distinguishing these responses is important for representing the optical consequences of BC aging in atmospheric models.

These findings should be interpreted within the intended scope of the modelling framework. The box-model experiments were designed to isolate process-specific responses under observation-constrained conditions rather than to reproduce the full spatial variability of the atmosphere. The idealized concentric core–shell representation does not explicitly resolve BC redistribution associated with liquid–liquid phase separation (Zhang et al., 2022) or coating-induced changes in particle morphology (Wei et al., 2024). Accordingly, the absolute values of E_{abs} reported here represent estimates under the adopted core–shell assumptions. Nevertheless, because the same optical treatment was applied consistently across all sensitivity simulations, the results provide a meaningful basis for comparing the responses of E_{abs} to different atmospheric processes. Future studies combining particle-resolved observations of BC morphology and coating structure with more realistic optical representations will help further evaluate these process-dependent relationships across different atmospheric environments.

https://doi.org/10.5194/egusphere-2026-5387
Preprint. Discussion started: 24 November 2026
© Author(s) 2026. CC BY 4.0 License.

Code and data availability

The elevation data were obtained from the GEBCO_2026 Grid (GEBCO Bathymetric Compilation Group 2026, 2026), available at https://doi.org/10.5285/4f68d5c7-45eb-f999-e063-7086abc036fa.
PartMC version 2.5.0, used for the simulations in this paper, is available at https://lagrange.mechse.illinois.edu/partmc/partmc-2.5.0.tar.gz.
The raw observational datasets used in this study have been deposited in Zenodo and can be freely downloaded from https://doi.org/10.5281/zenodo.22305774.
The codes used for data processing and figure generation have been deposited in a separate Zenodo repository and can be freely downloaded https://doi.org/10.5281/zenodo.22305914.

Author contributions

QM wrote the manuscript. QM, JS, TL, WL and GZ discussed the original idea and results.FS, XL, and ZZ conducted the field measurement. QM, YL and BA processed and analysed the data.

Competing interests

The authors declare that they have no conflict of interest.

Financial support

This study was financially supported by the National Natural Science Foundation of China (42405083) and the Fundamental Research Funds for the Central Universities (2025XYCM70).

References

Bond, T. C. and Bergstrom, R. W.: Light Absorption by Carbonaceous Particles: An Investigative Review, Aerosol Science and Technology, 40, 27–67, 10.1080/02786820500421521, 2006.
Bondy, A. L., Bonanno, D., Moffet, R. C., Wang, B., Laskin, A., and Ault, A. P.: The diverse chemical mixing state of aerosol particles in the southeastern United States, Atmos. Chem. Phys., 18, 12595–12612, 10.5194/acp-18-12595-2018, 2018.
Cappa, C. D., Zhang, X., Russell, L. M., Collier, S., Lee, A. K. Y., Chen, C. L., Betha, R., Chen, S., Liu, J., Price, D. J., Sanchez, K. J., McMeeking, G. R., Williams, L. R., Onasch, T. B., Worsnop, D. R., Abbatt, J., and Zhang, Q.: Light Absorption by Ambient Black and Brown Carbon and its Dependence on Black Carbon Coating State for Two California, USA, Cities in Winter and Summer, Journal of Geophysical Research: Atmospheres, 124, 1550–1577, 10.1029/2018jd029501, 2019.
Cappa, C. D., Onasch, T. B., Massoli, P., Worsnop, D. R., Bates, T. S., Cross, E. S., Davidovits, P., Hakala, J., Hayden, K. L., Jobson, B. T., Kolesar, K. R., Lack, D. A., Lerner, B. M., Li, S.-M., Mellon, D., Nuaaman, I., Olfert, J. S., Petäjä, T.,

https://doi.org/10.5194/egusphere-2026-5387
Preprint. Discussion started: 24 November 2026
© Author(s) 2026. CC BY 4.0 License.

Quinn, P. K., Song, C., Subramanian, R., Williams, E. J., and Zaveri, R. A.: Radiative Absorption Enhancements Due to the Mixing State of Atmospheric Black Carbon, Science, 337, 1078–1081, 10.1126/science.1223447, 2012.
Cheng, Y. F., Su, H., Rose, D., Gunthe, S. S., Berghof, M., Wehner, B., Achtert, P., Nowak, A., Takegawa, N., Kondo, Y., Shiraiwa, M., Gong, Y. G., Shao, M., Hu, M., Zhu, T., Zhang, Y. H., Carmichael, G. R., Wiedensohler, A., Andreae, M. O., and Pöschl, U.: Size-resolved measurement of the mixing state of soot in the megacity Beijing, China: diurnal cycle, aging and parameterization, Atmospheric Chemistry and Physics, 12, 4477–4491, 10.5194/acp-12-4477-2012, 2012.
Dickau, M., Olfert, J., Stettler, M. E. J., Boies, A., Momenimovahed, A., Thomson, K., Smallwood, G., and Johnson, M.: Methodology for quantifying the volatile mixing state of an aerosol, Aerosol Science and Technology, 50, 759–772, 10.1080/02786826.2016.1185509, 2016.
Farley, R. N., Lee, J. E., Rivellini, L. H., Lee, A. K. Y., Dal Porto, R., Cappa, C. D., Gorkowski, K., Shawon, A. S. M., Benedict, K. B., Aiken, A. C., Dubey, M. K., and Zhang, Q.: Chemical properties and single-particle mixing state of soot aerosol in Houston during the TRACER campaign, Atmos. Chem. Phys., 24, 3953–3971, 10.5194/acp-24-3953-2024, 2024.
Fierce, L., Bond, T. C., Bauer, S. E., Mena, F., and Riemer, N.: Black carbon absorption at the global scale is affected by particle-scale diversity in composition, in: Nat Commun, England, 12361, 10.1038/ncomms12361, 2016.
Fierce, L., Onasch, T. B., Cappa, C. D., Mazzoleni, C., China, S., Bhandari, J., Davidovits, P., Fischer, D. A., Helgestad, T., Lambe, A. T., Sedlacek, A. J., 3rd, Smith, G. D., and Wolff, L.: Radiative absorption enhancements by black carbon controlled by particle-to-particle heterogeneity in composition, in: Proc Natl Acad Sci U S A, United States, 5196–5203, 10.1073/pnas.1919723117, 2020.
Healy, R. M., Riemer, N., Wenger, J. C., Murphy, M., West, M., Poulain, L., Wiedensohler, A., O'Connor, I. P., McGillicuddy, E., Sodeau, J. R., and Evans, G. J.: Single particle diversity and mixing state measurements, Atmospheric Chemistry and Physics, 14, 6289–6299, 10.5194/acp-14-6289-2014, 2014.
Huang, X.-F., Peng, Y., Wei, J., Peng, J., Lin, X.-Y., Tang, M.-X., Cheng, Y., Men, Z., Fang, T., Zhang, J., He, L.-Y., Cao, L.-M., Liu, C., Zhang, C., Mao, H., Seinfeld, J. H., and Wang, Y.: Microphysical complexity of black carbon particles restricts their warming potential, One Earth, 7, 136–145, https://doi.org/10.1016/j.oneear.2023.12.004, 2024.
Janhäll, S., Andreae, M. O., and Pöschl, U.: Biomass burning aerosol emissions from vegetation fires: particle number and mass emission factors and size distributions, Atmos. Chem. Phys., 10, 1427–1439, 10.5194/acp-10-1427-2010, 2010.
Lee, A. K. Y., Rivellini, L.-H., Chen, C.-L., Liu, J., Price, D. J., Betha, R., Russell, L. M., Zhang, X., and Cappa, C. D.: Influences of Primary Emission and Secondary Coating Formation on the Particle Diversity and Mixing State of Black Carbon Particles, Environmental Science & Technology, 53, 9429–9438, 10.1021/acs.est.9b03064, 2019.
Li, J., Jiang, L., Chen, C., Liu, D., Du, S., Zhang, Y., Yang, Y., and Tang, L.: Characteristics and Sources of Black Carbon Aerosol in a Mega-City in the Western Yangtze River Delta, China, 10.3390/atmos11040315, 2020.
Li, J., Zhai, T., Chen, X., Wang, H., Xie, S., Chen, S., Li, C., Gong, Y., Dong, H., and Lu, K.: Direct measurement of N2O5 heterogeneous uptake coefficients on atmospheric aerosols in southwestern China and evaluation of current parameterizations, Atmospheric Chemistry and Physics, 25, 6395–6406, 10.5194/acp-25-6395-2025, 2025.
Li, K., Ye, X., Pang, H., Lu, X., Chen, H., Wang, X., Yang, X., Chen, J., and Chen, Y.: Temporal variations in the hygroscopicity and mixing state of black carbon aerosols in a polluted megacity area, Atmospheric Chemistry and Physics, 18, 15201–15218, 10.5194/acp-18-15201-2018, 2018.
Li, L., Hu, J., Li, J., Gong, K., Wang, X., Ying, Q., Qin, M., Liao, H., Guo, S., Hu, M., and Zhang, Y.: Modelling air quality during the EXPLORE-YRD campaign – Part II. Regional source apportionment of ozone and PM2.5, Atmospheric Environment, 247, 118063, https://doi.org/10.1016/j.atmosenv.2020.118063, 2021.
Liu, D., Allan, J. D., Young, D. E., Coe, H., Beddows, D., Fleming, Z. L., Flynn, M. J., Gallagher, M. W., Harrison, R. M., Lee, J., Prevot, A. S. H., Taylor, J. W., Yin, J., Williams, P. I., and Zotter, P.: Size distribution, mixing state and source apportionment of black carbon aerosol in London during wintertime, Atmospheric Chemistry and Physics, 14, 10061–10084, 10.5194/acp-14-10061-2014, 2014.
Liu, D., Whitehead, J., Alfarra, M. R., Reyes-Villegas, E., Spracklen, Dominick V., Reddington, Carly L., Kong, S., Williams, Paul I., Ting, Y.-C., Haslett, S., Taylor, Jonathan W., Flynn, Michael J., Morgan, William T., McFiggans, G., Coe, H., and Allan, James D.: Black-carbon absorption enhancement in the atmosphere determined by particle mixing state, Nature Geoscience, 10, 184–188, 10.1038/ngeo2901, 2017.

https://doi.org/10.5194/egusphere-2026-5387
Preprint. Discussion started: 24 November 2026
© Author(s) 2026. CC BY 4.0 License.

Liu, H., Pan, X., Lei, S., Zhang, Y., Du, A., Yao, W., Tang, G., Wang, T., Xin, J., Li, J., Sun, Y., Cao, J., and Wang, Z.: Vertical distribution of black carbon and its mixing state in the urban boundary layer in summer, Atmos. Chem. Phys., 23, 7225–7239, 10.5194/acp-23-7225-2023, 2023.

Liu, Y., Meng, X., Wu, Z., Huang, D., Wang, H., Chen, J., Chen, J., Zong, T., Fang, X., Tan, T., Zhao, G., Chen, S., Zeng, L., Guo, S., Huang, X., He, L., Zeng, L., and Hu, M.: The particle phase state during the biomass burning events, Science of The Total Environment, 792, 148035, https://doi.org/10.1016/j.scitotenv.2021.148035, 2021.

Ma, X., Tan, Z., Lu, K., Yang, X., Chen, X., Wang, H., Chen, S., Fang, X., Li, S., Li, X., Liu, J., Liu, Y., Lou, S., Qiu, W., Wang, H., Zeng, L., and Zhang, Y.: OH and HO2 radical chemistry at a suburban site during the EXPLORE-YRD campaign in 2018, Atmospheric Chemistry and Physics, 22, 7005–7028, 10.5194/acp-22-7005-2022, 2022.

Ni, H., Tian, J., Wang, X., Wang, Q., Han, Y., Cao, J., Long, X., Chen, L. W. A., Chow, J. C., Watson, J. G., Huang, R.-J., and Dusek, U.: PM2.5 emissions and source profiles from open burning of crop residues, Atmospheric Environment, 169, 229–237, https://doi.org/10.1016/j.atmosenv.2017.08.063, 2017.

O'Brien, R. E., Wang, B., Laskin, A., Riemer, N., West, M., Zhang, Q., Sun, Y., Yu, X.-Y., Alpert, P., Knopf, D. A., Gilles, M. K., and Moffet, R. C.: Chemical imaging of ambient aerosol particles: Observational constraints on mixing state parameterization, Journal of Geophysical Research: Atmospheres, 120, 9591–9605, https://doi.org/10.1002/2015JD023480, 2015.

Peng, J., Hu, M., Guo, S., Du, Z., Shang, D., Zheng, J., Zheng, J., Zeng, L., Shao, M., Wu, Y., Collins, D., and Zhang, R.: Ageing and hygroscopicity variation of black carbon particles in Beijing measured by a quasi-atmospheric aerosol evolution study (QUALITY) chamber, Atmospheric Chemistry and Physics, 17, 10333–10348, 10.5194/acp-17-10333-2017, 2017.

Peng, J., Hu, M., Guo, S., Du, Z., Zheng, J., Shang, D., Levy Zamora, M., Zeng, L., Shao, M., Wu, Y.-S., Zheng, J., Wang, Y., Glen, C. R., Collins, D. R., Molina, M. J., and Zhang, R.: Markedly enhanced absorption and direct radiative forcing of black carbon under polluted urban environments, Proceedings of the National Academy of Sciences, 113, 4266–4271, 10.1073/pnas.1602310113, 2016.

Riemer, N. and West, M.: Quantifying aerosol mixing state with entropy and diversity measures, Atmospheric Chemistry and Physics, 13, 11423–11439, 10.5194/acp-13-11423-2013, 2013.

Riemer, N., West, M., Zaveri, R. A., and Easter, R. C.: Simulating the evolution of soot mixing state with a particle-resolved aerosol model, Journal of Geophysical Research: Atmospheres, 114, https://doi.org/10.1029/2008JD011073, 2009.

Shiraiwa, M., Kondo, Y., Moteki, N., Takegawa, N., Miyazaki, Y., and Blake, D. R.: Evolution of mixing state of black carbon in polluted air from Tokyo, Geophysical Research Letters, 34, 10.1029/2007gl029819, 2007.

Shiraiwa, M., Kondo, Y., Moteki, N., Takegawa, N., Sahu, L. K., Takami, A., Hatakeyama, S., Yonemura, S., and Blake, D. R.: Radiative impact of mixing state of black carbon aerosol in Asian outflow, Journal of Geophysical Research: Atmospheres, 113, 10.1029/2008jd010546, 2008.

Shou, C., Riemer, N., Onasch, T. B., Sedlacek, A. J., Lambe, A. T., Lewis, E. R., Davidovits, P., and West, M.: Mixing state evolution of agglomerating particles in an aerosol chamber: Comparison of measurements and particle-resolved simulations, Aerosol Science and Technology, 53, 1229–1243, 10.1080/02786826.2019.1661959, 2019.

Sun, J., Zhao, G., Yu, J., Lin, W., Chen, Y., Ye, C., Fang, W., Zhou, W., Zhu, B., Yang, J., Wu, Z., Liu, T., Gao, Y., Shen, F., and Zhu, T.: Amplified radiative effects of coated black carbon aerosols over the Tibetan Plateau, Atmospheric Research, 331, 108678, https://doi.org/10.1016/j.atmosres.2025.108678, 2026.

Tan, T., Hu, M., Du, Z., Zhao, G., Shang, D., Zheng, J., Qin, Y., Li, M., Wu, Y., Zeng, L., Guo, S., and Wu, Z.: Measurement report: Strong light absorption induced by aged biomass burning black carbon over the southeastern Tibetan Plateau in pre-monsoon season, Atmos. Chem. Phys., 21, 8499–8510, 10.5194/acp-21-8499-2021, 2021.

Tao, J., Luo, B., Xu, W., Zhao, G., Xu, H., Xue, B., Zhai, M., Xu, W., Zhao, H., Ren, S., Zhou, G., Liu, L., Kuang, Y., and Sun, Y.: Markedly different impacts of primary emissions and secondary aerosol formation on aerosol mixing states revealed by simultaneous measurements of CCNC, H(/V)TDMA, and SP2, Atmospheric Chemistry and Physics, 24, 9131–9154, 10.5194/acp-24-9131-2024, 2024.

Tao, J. C., Zhao, C. S., Ma, N., and Liu, P. F.: The impact of aerosol hygroscopic growth on the single-scattering albedo and its application on the NO2 photolysis rate coefficient, Atmospheric Chemistry and Physics, 14, 12055–12067, 10.5194/acp-14-12055-2014, 2014.

https://doi.org/10.5194/egusphere-2026-5387
Preprint. Discussion started: 24 November 2026
© Author(s) 2026. CC BY 4.0 License.

Tian, J., Brem, B. T., West, M., Bond, T. C., Rood, M. J., and Riemer, N.: Simulating aerosol chamber experiments with the particle-resolved aerosol model PartMC, Aerosol Science and Technology, 51, 856–867, 10.1080/02786826.2017.1311988, 2017.
Wang, H., Chen, X., Lu, K., Hu, R., Li, Z., Wang, H., Ma, X., Yang, X., Chen, S., Dong, H., Liu, Y., Fang, X., Zeng, L., Hu, M., and Zhang, Y.: NO3 and N2O5 chemistry at a suburban site during the EXPLORE-YRD campaign in 2018, Atmospheric Environment, 224, 117180, https://doi.org/10.1016/j.atmosenv.2019.117180, 2020.
Wang, J., Zhang, Q., Chen, M., Collier, S., Zhou, S., Ge, X., Xu, J., Shi, J., Xie, C., Hu, J., Ge, S., Sun, Y., and Coe, H.: First Chemical Characterization of Refractory Black Carbon Aerosols and Associated Coatings over the Tibetan Plateau (4730 m a.s.l), Environ Sci Technol, 51, 14072–14082, 10.1021/acs.est.7b03973, 2017.
Wang, Y., Li, W., Huang, J., Liu, L., Pang, Y., He, C., Liu, F., Liu, D., Bi, L., Zhang, X., and Shi, Z.: Nonlinear Enhancement of Radiative Absorption by Black Carbon in Response to Particle Mixing Structure, Geophysical Research Letters, 48, 10.1029/2021gl096437, 2021.
Wei, X., Hu, J., Liu, C., Xie, X., Yin, J., Guo, S., Hu, M., Peng, J., and Wang, H.: Advanced modeling of the absorption enhancement of black carbon particles in chamber experiments by considering the morphology and coating thickness, Frontiers of Environmental Science & Engineering, 18, 116, 10.1007/s11783-024-1876-4, 2024.
Wu, J., Liu, J., Gunsch, M. J., Mirrielees, J. A., Moffett, C. E., Zhang, Q., Sheesley, R. J., and Pratt, K. A.: Quantifying the Diversity of an Atmospheric Aerosol Population in an Arctic Oil Field on a Single-Particle Level, Journal of Geophysical Research: Atmospheres, 129, e2024JD041001, https://doi.org/10.1029/2024JD041001, 2024.
Wu, Y., Cheng, T., Liu, D., Allan, J. D., Zheng, L., and Chen, H.: Light Absorption Enhancement of Black Carbon Aerosol Constrained by Particle Morphology, Environ Sci Technol, 52, 6912–6919, 10.1021/acs.est.8b00636, 2018.
Xu, X., Zhao, W., Qian, X., Wang, S., Fang, B., Zhang, Q., Zhang, W., Venables, D. S., Chen, W., Huang, Y., Deng, X., Wu, B., Lin, X., Zhao, S., and Tong, Y.: The influence of photochemical aging on light absorption of atmospheric black carbon and aerosol single-scattering albedo, Atmos. Chem. Phys., 18, 16829–16844, 10.5194/acp-18-16829-2018, 2018.
Yao, Y., Curtis, J. H., Ching, J., Zheng, Z., and Riemer, N.: Quantifying the effects of mixing state on aerosol optical properties, Atmospheric Chemistry and Physics, 22, 9265–9282, 10.5194/acp-22-9265-2022, 2022.
Yu, C., Liu, D., Broda, K., Joshi, R., Olfert, J., Sun, Y., Fu, P., Coe, H., and Allan, J. D.: Characterising mass-resolved mixing state of black carbon in Beijing using a morphology-independent measurement method, Atmospheric Chemistry and Physics, 20, 3645–3661, 10.5194/acp-20-3645-2020, 2020.
Yuan, C., Zheng, J., Ma, Y., Jiang, Y., Li, Y., and Wang, Z.: Significant restructuring and light absorption enhancement of black carbon particles by ammonium nitrate coating, Environmental Pollution, 262, 114172, https://doi.org/10.1016/j.envpol.2020.114172, 2020.
Zaveri, R. A., Easter, R. C., and Peters, L. K.: A computationally efficient Multicomponent Equilibrium Solver for Aerosols (MESA), Journal of Geophysical Research: Atmospheres, 110, https://doi.org/10.1029/2004JD005618, 2005a.
Zaveri, R. A., Easter, R. C., and Wexler, A. S.: A new method for multicomponent activity coefficients of electrolytes in aqueous atmospheric aerosols, Journal of Geophysical Research: Atmospheres, 110, https://doi.org/10.1029/2004JD004681, 2005b.
Zaveri, R. A., Easter, R. C., Fast, J. D., and Peters, L. K.: Model for Simulating Aerosol Interactions and Chemistry (MOSAIC), Journal of Geophysical Research: Atmospheres, 113, https://doi.org/10.1029/2007JD008782, 2008.
Zaveri, R. A., Barnard, J. C., Easter, R. C., Riemer, N., and West, M.: Particle-resolved simulation of aerosol size, composition, mixing state, and the associated optical and cloud condensation nuclei activation properties in an evolving urban plume, Journal of Geophysical Research: Atmospheres, 115, https://doi.org/10.1029/2009JD013616, 2010.
Zeng, L., Tan, T., Zhao, G., Du, Z., Hu, S., Shang, D., and Hu, M.: Overestimation of black carbon light absorption due to mixing state heterogeneity, npj Climate and Atmospheric Science, 7, 10.1038/s41612-023-00535-8, 2024.
Zha, S., Cheng, T., Tao, J., Zhang, R., Chen, J., Zhang, Y., Leng, C., Zhang, D., and Du, J.: Characteristics and relevant remote sources of black carbon aerosol in Shanghai, Atmospheric Research, 135-136, 159–171, https://doi.org/10.1016/j.atmosres.2013.09.002, 2014.
Zhai, J., Yang, X., Li, L., Bai, B., Liu, P., Huang, Y., Fu, T.-M., Zhu, L., Zeng, Z., Tao, S., Lu, X., Ye, X., Wang, X., Wang, L., and Chen, J.: Absorption Enhancement of Black Carbon Aerosols Constrained by Mixing-State Heterogeneity, Environmental Science & Technology, 56, 1586–1593, 10.1021/acs.est.1c06180, 2022.

https://doi.org/10.5194/egusphere-2026-5387
Preprint. Discussion started: 24 November 2026
© Author(s) 2026. CC BY 4.0 License.



Zhang, J., Wang, Y., Teng, X., Liu, L., Xu, Y., Ren, L., Shi, Z., Zhang, Y., Jiang, J., Liu, D., Hu, M., Shao, L., Chen, J., Martin, S. T., Zhang, X., and Li, W.: Liquid-liquid phase separation reduces radiative absorption by aged black carbon aerosols, Communications Earth & Environment, 3, 128, 10.1038/s43247-022-00462-1, 2022.

Zhang, L., Sun, J. Y., Shen, X. J., Zhang, Y. M., Che, H., Ma, Q. L., Zhang, Y. W., Zhang, X. Y., and Ogren, J. A.: Observations of relative humidity effects on aerosol light scattering in the Yangtze River Delta of China, Atmospheric Chemistry and Physics, 15, 8439–8454, 10.5194/acp-15-8439-2015, 2015.

Zhang, Y., Su, H., Ma, N., Li, G., Kecorius, S., Wang, Z., Hu, M., Zhu, T., He, K., Wiedensohler, A., Zhang, Q., and Cheng, Y.: Sizing of Ambient Particles From a Single-Particle Soot Photometer Measurement to Retrieve Mixing State of Black Carbon at a Regional Site of the North China Plain, Journal of Geophysical Research: Atmospheres, 123, 10.1029/2018jd028810, 2018.

Zhang, Z., Wang, J., Wang, J., Riemer, N., Liu, C., Jin, Y., Tian, Z., Cai, J., Cheng, Y., Chen, G., Wang, B., Wang, S., and Ding, A.: Steady-state mixing state of black carbon aerosols from a particle-resolved model, Atmospheric Chemistry and Physics, 25, 1869–1881, 10.5194/acp-25-1869-2025, 2025.

Zhao, G., Tan, T., Zhu, Y., Hu, M., and Zhao, C.: Method to quantify black carbon aerosol light absorption enhancement with a mixing state index, Atmospheric Chemistry and Physics, 21, 18055–18063, 10.5194/acp-21-18055-2021, 2021.

Zhao, G., Tan, T., Zhao, W., Guo, S., Tian, P., and Zhao, C.: A new parameterization scheme for the real part of the ambient urban aerosol refractive index, Atmos. Chem. Phys., 19, 12875–12885, 10.5194/acp-19-12875-2019, 2019.

Zhao, G., Tan, T., Hu, S., Du, Z., Shang, D., Wu, Z., Guo, S., Zheng, J., Zhu, W., Li, M., Zeng, L., and Hu, M.: Mixing state of black carbon at different atmospheres in north and southwest China, Atmos. Chem. Phys., 22, 10861–10873, 10.5194/acp-22-10861-2022, 2022.

Zhao, W., Li, Y., Zhao, G., Guo, S., Ma, N., Hu, S., and Zhao, C.: Measurement report: Size-resolved mass concentration of equivalent black carbon-containing particles larger than 700 nm and their role in radiation, Atmos. Chem. Phys., 23, 14889–14902, 10.5194/acp-23-14889-2023, 2023.